Dependence of diffusion in *Escherichia coli* cytoplasm on protein size, environmental conditions and cell growth

N. Bellotto[1], J. Agudo-Canalejo[2,†], R. Colin[1,†], R. Golestanian[2,3,+], G. Malengo[1,+], V. Sourjik[1,+]

[1]Max Planck Institute for Terrestrial Microbiology and LOEWE Center for Synthetic Microbiology (SYNMIKRO), Karl-von-Frisch-Strasse 16, D-35043 Marburg, Germany

[2]Max Planck Institute for Dynamics and Self-Organization, Am Faßberg 17, D-37077 Göttingen, Germany

[3]Rudolf Peierls Centre for Theoretical Physics, University of Oxford, Oxford OX1 3PU, United Kingdom

[†]These authors equally contributed to this work

[+]Corresponding authors: ramin.golestanian@ds.mpg.de, gabriele.malengo@synmikro.mpi-marburg.mpg.de, victor.sourjik@synmikro.mpi-marburg.mpg.de

Abstract

Inside prokaryotic cells, passive translational diffusion typically limits the rates with which cytoplasmic proteins can reach their locations and interact with partners. Diffusion is thus fundamental to most cellular processes, but the understanding of protein mobility in the highly crowded and non-homogeneous environment of a bacterial cell is still limited. Here we investigated the mobility of a large set of proteins in the cytoplasm of *Escherichia coli*, by employing fluorescence correlation spectroscopy (FCS) combined with simulations and theoretical modeling. We conclude that cytoplasmic protein mobility could be well described by Brownian diffusion in the confined geometry of the bacterial cell and at high viscosity imposed by macromolecular crowding. The size dependence of protein diffusion is well consistent with the Stokes-Einstein relation for small fusion proteins when taking into account their shape, but larger proteins diffuse slower than expected from this relation. Pronounced subdiffusion and hindered mobility is observed for proteins with extensive interactions within the cytoplasm. Finally, we show that cytoplasmic viscosity has a temperature dependence comparable to that of water, and that protein mobility is increased by biosynthetic activity and cell growth.

32 # Introduction

33 Diffusion of molecules is important for the function of any cellular system, setting the upper limit
34 for mobility of proteins and other (macro)molecules and for the rates of many biochemical
35 reactions that rely on random encounters between molecules (Schavemaker, Boersma, and
36 Poolman 2018). Although the fundamental physics of diffusion in dilute aqueous solutions is well
37 understood and mathematically described (Einstein 1906; Langevin 1908; Perrin 1909), diffusion
38 in a cellular environment may be quite different (Schavemaker, Boersma, and Poolman 2018; Mika
39 and Poolman 2011). The concentration of macromolecules in the bacterial cytoplasm, primarily
40 proteins but also ribonucleic acids (RNAs), is extremely high. For *Escherichia coli*, it is around
41 300 mg/mL, which corresponds to a volume fraction of 25-30% (Cayley et al. 1991; Zimmerman
42 and Trach 1991). Such macromolecular crowding could hinder free diffusion and influence
43 kinetics of protein association and of gene expression (Klumpp et al. 2013; Tabaka et al. 2014;
44 van den Berg, Boersma, and Poolman 2017). The effects of crowding on protein diffusion have
45 been demonstrated both *in vitro* and *in vivo* (Dix and Verkman 2008; Rivas and Minton 2016).
46 Compared to water, the diffusion of a free green fluorescent protein (GFP) was reported to be three
47 to four times slower in the eukaryotic cytoplasm (Swaminathan, Hoang, and Verkman 1997) and
48 up to ten times slower in the bacterial cytoplasm (Elowitz Michael et al. 1999; Nenninger,
49 Mastroianni, and Mullineaux 2010; Mika et al. 2010; Kumar, Mommer, and Sourjik 2010).

50 In addition to the high density of macromolecules, the diversity in the size and chemical properties
51 of the solutes makes the cytoplasmic environment highly inhomogeneous (Luby-Phelps 1999;
52 Spitzer and Poolman 2013). How much the diffusion of a particular molecule is affected by
53 macromolecular crowding might thus depend on the size (Muramatsu and Minton 1988) and shape
54 of the molecule (Balbo et al. 2013) as well as on the nature of the crowders (Banks and Fradin

55 2005; Goins, Sanabria, and Waxham 2008). The effects of crowding observed in living cells appear
56 to be even more complex, varying not only with the diffusing particle but also with the
57 physiological state of the cell (Parry et al. 2014; Joyner et al. 2016) and the local cellular
58 environment (Konopka et al. 2006; Persson, Ambati, and Brandman 2020). Moreover, non-trivial
59 effects on diffusion arise due to reversible assembly and disassembly of the diffusing protein
60 complexes (Agudo-Canalejo, Illien, and Golestanian 2020), and possibly also due to the active
61 enhancement of enzyme diffusion by catalytic reactions (Golestanian 2015; Agudo-Canalejo et
62 al. 2018; Zhang and Hess 2019).

63 The dependence of the diffusion coefficient (D) of a protein in the cytoplasm on its size might thus
64 not necessarily follow the Stokes-Einstein (also called Stokes-Einstein-Sutherland-
65 Smoluchowski) relation that is valid in dilute solutions, $D \propto T/(\eta R)$ (Einstein 1906), where T is
66 absolute temperature in Kelvin, η is the viscosity of the medium and R is the hydrodynamic radius
67 of the particle. For globular proteins, R is given by the radius of gyration (Tyn and Gusek 1990)
68 and depends on the molecular mass (MM) as $R \propto \mathrm{MM}^{\beta}$, where the exponent β would be 1/3 for
69 perfectly compact and globular proteins but is in practice within the range of 0.35-0.43 for typical
70 proteins, reflecting the fractal nature of the spatial distribution of protein mass (Smilgies and Folta-
71 Stogniew 2015; Enright and Leitner 2005). Several studies of protein diffusion in the cytoplasm
72 of *E. coli* have yielded different dependencies on the molecular mass, with an average $\beta \sim 0.7$
73 estimated based on the data pooled from multiple studies (Nenninger, Mastroianni, and Mullineaux
74 2010; Kumar, Mommer, and Sourjik 2010; Mika and Poolman 2011; Kalwarczyk, Tabaka, and
75 Holyst 2012), and thus substantially steeper than predicted by the Stokes-Einstein relation. Similar
76 exponent of ~0.7 was observed for a limited set of differently-sized proteins (Mika et al. 2010;
77 Stracy et al. 2021). However, neither of these studies took explicitly into account the non-

78 globularity of the used fluorescent constructs, where two or more proteins are typically connected
79 by flexible linkers. For such multidomain proteins, shape fluctuations and hydrodynamic
80 interactions between the different domains can have a sizeable effect on the effective diffusion
81 coefficient of the whole protein (Agudo-Canalejo and Golestanian 2020).

82 Besides macromolecular crowding, the translational diffusion of cytoplasmic proteins is also
83 influenced by intracellular structures, such as cytoskeletal filaments (Sabri et al. 2020), and by
84 (transient) binding to other macromolecules (Guigas and Weiss 2008; Saxton 2007). Both these
85 factors can not only reduce protein mobility but also lead to the anomalous subdiffusive behavior,
86 where the mean square displacement (MSD) of diffusing particles does not scale linearly with
87 time, as for Brownian diffusion in dilute solutions, but rather follows MSD $\propto t^{\alpha}$ with the anomalous
88 diffusion exponent α being <1 (Saxton 1996; Etoc et al. 2018). Subdiffusion is commonly observed
89 in eukaryotes, particularly at longer spatial scales, primarily due to the obstruction by the
90 cytoskeletal filaments (Di Rienzo et al. 2014; Sabri et al. 2020). Mobility of mRNA molecules in
91 the bacterial cytoplasm is also subdiffusive (Golding and Cox 2004; Lampo et al. 2017). In
92 contrast, the diffusion of several tested cytoplasmic bacterial proteins was apparently Brownian
93 (Bakshi, Bratton, and Weisshaar 2011; English et al. 2011).

94 Even for the same protein, e.g. GFP or its spectral variants, estimates of the diffusion coefficient
95 in the cytoplasm obtained in different studies vary widely (Schavemaker, Boersma, and Poolman
96 2018), which could be in part due to differences in methodologies. Most early studies in bacteria
97 relied on fluorescence recovery after photobleaching (FRAP), where diffusion is quantified from
98 the recovery of fluorescence in a region of the cell bleached by a high intensity laser (Loren et al.
99 2015). These measurements provided values of diffusion coefficient for GFP ranging from 3 $\mu m^2 s^{-1}$
100 to 14 $\mu m^2 s^{-1}$ (Elowitz Michael et al. 1999; Mullineaux et al. 2006; Konopka et al. 2009; Kumar,

101 Mommer, and Sourjik 2010; Mika et al. 2010; Nenninger, Mastroianni, and Mullineaux 2010;
102 Schavemaker, Smigiel, and Poolman 2017). More recently, single-particle tracking (SPT), where
103 diffusion is measured by following the trajectories of single fluorescent molecules over time
104 (Kapanidis, Uphoff, and Stracy 2018), became increasingly used. Lastly, diffusion can also be
105 studied *in vivo* using fluorescence correlation spectroscopy (FCS) (Cluzel, Surette, and Leibler
106 2000), which measures the time required by a fluorescent molecule to cross the observation volume
107 of a confocal microscope (Elson 2011). SPT and FCS measure protein mobility locally within the
108 cell, with FCS having also a significantly better temporal resolution than FRAP and SPT. Both
109 methods provided higher but still varying values of D_{GFP}, from 8 $\mu m^2 s^{-1}$ up to 18 $\mu m^2 s^{-1}$ (Meacci
110 et al. 2006; English et al. 2011; Sanamrad et al. 2014; Diepold et al. 2017; Rocha et al. 2019).

111 Protein mobility also depends on the environmental and cellular conditions that affect the structure
112 of the cytoplasm (Schavemaker, Boersma, and Poolman 2018). Previously studied examples
113 include effects of high osmolarity that increases macromolecular crowding and creates diffusion
114 barriers (Konopka et al. 2006; Konopka et al. 2009; Liu et al. 2019) and of the energy-dependent
115 fluidization of the cytoplasm to enable diffusion of large particles (Parry et al. 2014). Furthermore,
116 the surface charge of cytoplasmic proteins has been shown to have a dramatic effect on their
117 mobility (Schavemaker, Smigiel, and Poolman 2017).

118 Variations between values of diffusion coefficients observed even for the same model organism in
119 different studies, each investigating only a limited number of protein probes, using different
120 strains, growth conditions and measurement techniques, hampered drawing general conclusions
121 about the effective viscosity of bacterial cytoplasm and its dependence on the protein size. Here,
122 we address these limitations by systematically analyzing the mobility of a large number of
123 differently-sized cytoplasmic fluorescent protein constructs under standardized conditions by FCS.

124 We further combined experiments with Brownian dynamics simulations and theoretical modeling
125 of diffusion to correct for effects of confined cell geometry. For the majority of studied constructs,
126 we observe a uniform dependence of the diffusion coefficient on the protein size, with a
127 pronounced upper limit on diffusion at a given molecular mass. When corrected for the
128 confinement due to the bacterial cell geometry, the diffusion of these constructs was nearly
129 Brownian. Moreover, part of the deviation of the mass-dependence of their diffusion coefficients
130 from the Stokes-Einstein relation might be explained by the specific shape of the fusion proteins.
131 An aberrantly slow and anomalous diffusion of several protein constructs was apparently due to
132 their strong interactions with other cellular proteins and protein complexes, and disruption of these
133 interactions restored a Brownian diffusion close to the upper limit expected for their mass. We
134 further investigated the dependence of protein mobility on environmental temperature, on
135 exposure to antibiotics and on cellular growth, and we tested the mobility of proteins that are non-
136 native to *E. coli*. Finally, we show that under the same experimental conditions FCS and FRAP
137 measurements yield similar values of diffusion coefficients, suggesting that, in contrast to
138 eukaryotic cells (Di Rienzo et al. 2014), no pronounced dependence of protein mobility on spatial
139 scale could be observed in the bacterial cytoplasm.

140

141 # Results

142 ## Dependence of cytoplasmic protein mobility on molecular mass measured by
143 FCS

144 For our analysis of cytoplasmic protein mobility, we generated a plasmid-encoded library of 31
145 cytoplasmic proteins (Figure 1 – supplementary table 1 and supplementary table 2) of *E. coli* fused

146 to superfolder GFP (sfGFP) (Pédelacq et al. 2006). We selected monomeric proteins with known
147 and roughly globular protein structure, to avoid effects on mobility due to multimerization or
148 irregular shape of proteins. These proteins belong to different cellular pathways, but DNA-binding
149 proteins were excluded. The expected size and stability of each construct was verified by gel
150 electrophoresis and immunoblotting (Figure 1 – figure supplement 1). Only one of the constructs,
151 ThpR-sfGFP, showed >20% degradation to free sfGFP, and it was therefore excluded from further
152 analyses. This was also the sole construct with an atypically high isoelectric point (pI), and all
153 remaining constructs have pI ranging from 5.1 to 6.2, as common for cytoplasmic proteins
154 (Schwartz, Ting, and King 2001). We further imaged the distribution of fusion proteins in the
155 cytoplasm. Except for RihA-sfGFP and NagD-sfGFP that were subsequently excluded, all other
156 constructs showed uniform localization (Figure 1A).
157 The mobility of the remaining 28 fusion constructs and of free sfGFP was investigated in living *E.*
158 *coli* cells by FCS (see Materials and Methods and Appendix 1). In order to facilitate the
159 measurements, cells were treated with the division inhibitor cephalexin for 45 min to induce
160 moderate elongation, yielding final cell length of ~ 5 μm (Figure 1A). During an FCS
161 measurement, the laser focus was positioned close to the polar region in the cell cytoplasm, and
162 the fluorescence intensity in the confocal volume was measured over time (Figure 1 – figure
163 supplement 2). For each individual cell, six subsequent acquisitions of 20 s each were performed
164 at the same position. The autocorrelation function (ACF) of the fluorescence intensity fluctuations
165 was independently calculated for each time interval and fitted to extract the mobility parameters
166 of the fluorescent proteins. Although we initially considered both the Brownian diffusion and the
167 anomalous diffusion models, the latter model proved to be considerably better in fitting the
168 experimental data (Figure 1 – figure supplement 3). The anomalous diffusion model was therefore

169 used to determine the diffusion (or residence) time (τ_D) of a fluorescent molecule in the confocal
170 volume and the anomalous diffusion exponent α for all ACFs (Figure 1B and Figure 1 –
171 supplementary table 1 and figure supplement 2). The averaged values of τ_D and α for each
172 individual cell were then calculated from these six individual acquisitions (Figure 1C and Figure
173 1 – figure supplement 4).

174 Despite their substantial intercellular variability, thus obtained mean values of the diffusion time
175 were clearly different between protein constructs (Figure 1C and Figure 1 – supplementary table
176 1. We next plotted the mean values of $1/\tau_D$, which reflect protein mobility, against the molecular
177 mass of protein constructs (Figure 1D). This dependence revealed a clear trend, where mobility of
178 more than half of the constructs decreased uniformly with their molecular mass, while some
179 exhibited much lower mobility than the other constructs of similar mass. In contrast, the anomalous
180 diffusion exponent α showed no apparent dependence on the protein size, ranging from 0.8 to 0.86
181 for most of the constructs (Figure 1E). Notably, the few protein constructs with α of ~ 0.8 or lower
182 were also among the ones with low mobility (Figure 1D and 1E, colored symbols).

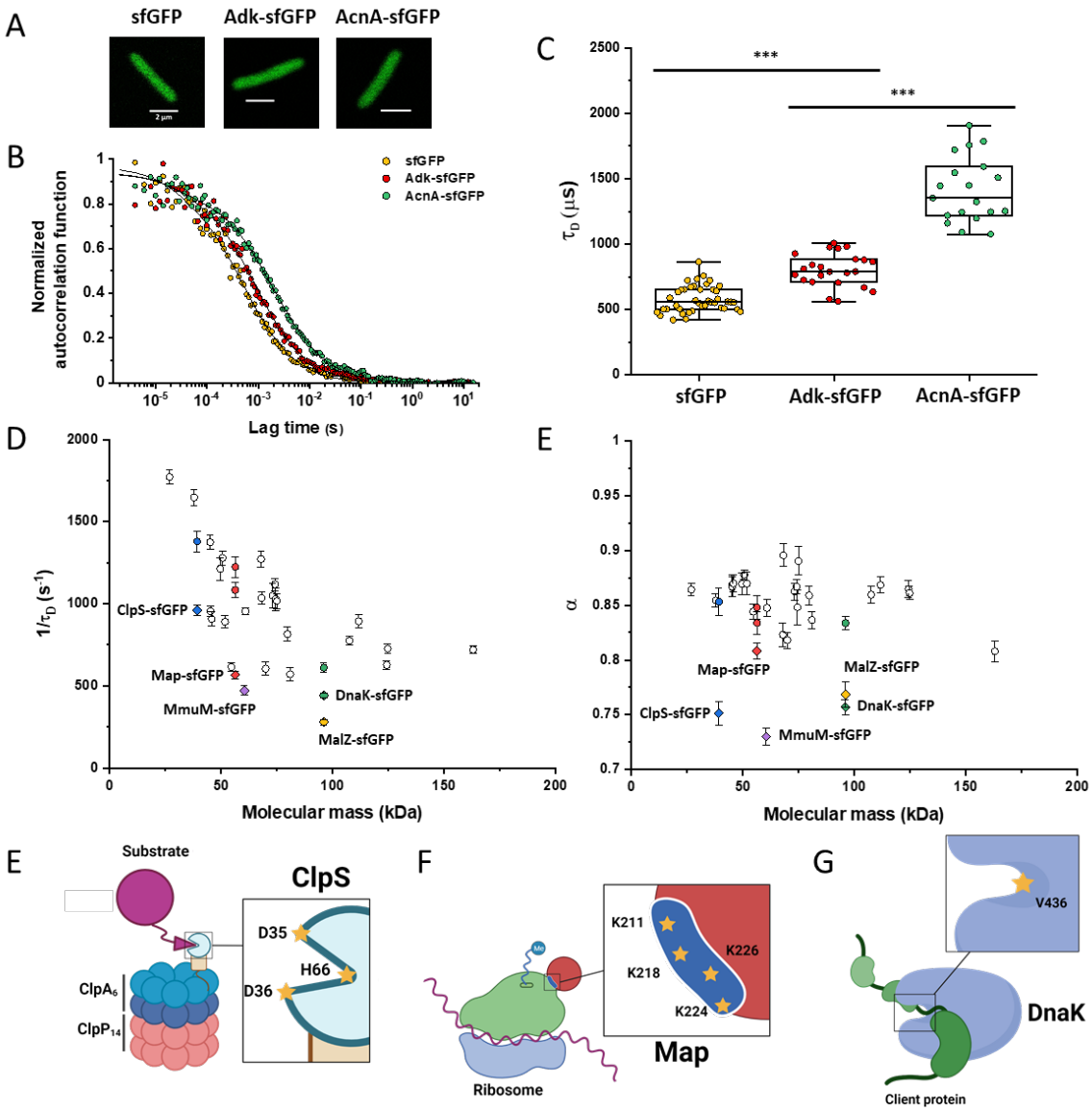

Figure 1. Dependence of protein mobility in bacterial cytoplasm on molecular mass and cellular interactions. (A) Examples of fluorescence microscopy images of *E. coli* cells expressing either sfGFP or the indicated sfGFP-tagged cytoplasmic proteins. Scale bar is 2 µm. (B) Representative autocorrelation functions (ACFs) measured by FCS for the indicated protein constructs. Data were fitted using the anomalous diffusion model (solid lines). All ACF curves were normalized to their respective maximal values to facilitate comparison. (C) Diffusion times (τ_D) measured for the indicated protein constructs. Each dot in the box plot represents the value for one individual cell, averaged over six consecutive acquisitions (Figure 1 – figure supplement 2) *** $p<0.0001$ in a two-tailed heteroscedastistic *t*-test. Exact p-values for all significance analyses performed in this study could be found in Appendix 4. (D, E). Dependence of protein mobility ($1/\tau_D$) (D) and apparent anomaly of diffusion (α) (E) on molecular mass. Each symbol represents

193 the average value for all individual cells that have been measured for that particular construct and the error bars
194 represent the standard error of the mean. Individual values are shown in Figure 1 – figure supplement 4 and the
195 numbers of measured cells are shown in Appendix 5. Protein constructs with most aberrant mobility are highlighted
196 in color and labeled. For fusions to ClpS, Map and DnaK, the values of $1/\tau_D$ and α for both original constructs
197 (diamonds) and constructs where mutations were introduced to disrupt interactions (circles) are shown. For Map, two
198 alternative amino acid substitutions that disrupt its interaction with the ribosome are shown (see Figure 1 – figure
199 supplement 6). (F-H) Cartoons illustrating the cellular interactions that could affect mobility of ClpS (F), Map (G),
200 and DnaK (H). ClpS engages with the ClpAP protease and with substrates, cartoon adapted from (Roman-Hernandez
201 et al. 2011). Map interacts with the actively translating ribosomes, cartoon adapted from (Sandikci et al. 2013). DnaK
202 interacts with unfolded client protein. Amino acidic residues that were mutated to disrupt interactions are highlighted
203 (see text for details).

204 **Figure 1 – source data 1.** Original values used for plots in Figure 1C-E.

205

206 Macromolecular interactions reduce protein mobility

207 We reasoned that the main group of constructs that exhibit mobility close to the apparent mass-
208 dependent upper limit represents proteins whose diffusion is only limited by macromolecular
209 crowding, and that the aberrantly low $1/\tau_D$ and α of other constructs might be due to their specific
210 interactions with other cellular proteins or protein complexes. Indeed, for three of these proteins
211 (ClpS, Map, DnaK) such interactions are well characterized and can be specifically disrupted. ClpS
212 is the adaptor protein that delivers degradation substrates to the protease ClpAP (Roman-
213 Hernandez et al. 2011). The substrate-binding site of ClpS is constituted by three amino acid
214 residues (D35, D36, H66) that interact with the N-terminal degron of target proteins (Figure 1F).
215 If these residues are mutated into alanine, substrate binding *in vitro* is substantially reduced
216 (Roman-Hernandez et al. 2011; Humbard et al. 2013). Additionally, ClpS directly docks to the
217 hexameric ClpA. Consistently, we observed that while stability of the mutant construct

218 ClpS^{D35A_D36A_H66A}-sfGFP was not affected (Figure 1 – figure supplement 5), its mobility in a
219 *ΔclpA* strain became significantly higher and less anomalous, with both $1/\tau_D$ and α reaching levels
220 similar to those of other proteins of similar mass (Figure 1D and 1E and Figure 1 – figure
221 supplement 6).

222 Similar results were obtained for the other two constructs. Map is the methionine aminopeptidase
223 that cleaves the N-terminal methionine from nascent polypeptide chains (Solbiati et al. 1999). Map
224 interacts with the negatively charged backbone of ribosomes through four positively charged
225 lysine residues (K211, 218, 224, 226) located in a loop (Figure 1G). If these residues are mutated
226 into alanine, the *in vitro* affinity of Map for the ribosomes is reduced (Sandikci et al. 2013). The
227 mobility of Map-sfGFP was indeed much increased by alanine substitutions at all four lysine sites
228 (Figure 1D and 1E and Figure 1 – figure supplement 5 and figure supplement 6). Interestingly,
229 charge inversion of lysines to glutamic acid did not further increase Map-sfGFP mobility as was
230 expected based on *in vitro* experiments (Sandikci et al. 2013).

231 DnaK is the major bacterial chaperone that binds to short hydrophobic polypeptide sequences,
232 which become exposed during protein synthesis, membrane translocation or protein unfolding
233 (Genevaux, Georgopoulos, and Kelley 2007). DnaK accommodates its substrate peptides inside a
234 hydrophobic pocket (Figure 1H). The substitution of the valine residue 436 with bulkier
235 phenylalanine creates steric hindrance that markedly decreases substrate binding to DnaK *in vitro*
236 (Mayer, Rüdiger, and Bukau 2000), and both the $1/\tau_D$ and α of DnaK^{V436F}-sfGFP were significantly
237 higher than for the correspondent wild-type construct (Figure 1D and 1E and Figure 1 – figure
238 supplement 5 and figure supplement 6). Nevertheless, in this case the $1/\tau_D$ did not reach the levels
239 of other proteins of similar molecular mass, which is likely explained by multiple interactions of

240 DnaK with other components of the cellular protein quality control machinery besides its binding
241 to substrates (Kumar and Sourjik 2012).

242

243 Cytoplasmic diffusion rate is conserved between bacterial species

244 We then investigated whether sfGFP fusions to non-native proteins, originating from other
245 bacteria, may show diffusion different from that of their *E. coli* counterparts. The existence of an
246 organism-dependent "quinary" code of unspecific, short living interactions has been recently
247 proposed in order to explain reduced mobility of heterologous human proteins in *E. coli* cytoplasm
248 (Mu et al. 2017). Thus, we investigated the mobility of proteins from other Gram-negative
249 proteobacteria *Yersinia enterocolitica*, *Vibrio cholerae*, *Caulobacter crescentus*, *Myxococcus*
250 *xanthus* and from the Gram-positive bacterium *Bacillus subtilis* that are homologous to several
251 freely-diffusing *E. coli* protein constructs (Figure 1 – figure supplement 7). Within this set of
252 constructs, we observed no significant differences of $1/\tau_D$ values from their *E. coli* counterparts,
253 except for AcnA from *M. xanthus* (Figure 1 – figure supplement 7A, C). Such lower mobility
254 might be a sign of multimerization of *M. xanthus* AcnA, although cellular distribution of this
255 construct was uniform. In contrast, most of these constructs showed slightly but significantly
256 increased anomaly of diffusion (Figure 1 – figure supplement 7B, D), which might reflect
257 increased "stickiness" of non-native proteins in *E. coli* cytoplasm.

258

259 Apparent anomaly of diffusion could be largely explained by confinement

260 When FCS measurements are performed in a confined space with dimensions comparable to those
261 of the observation volume, such confinement may affect the apparent mobility of fluorescent

262 molecules (Gennerich and Schild 2000; Jiang et al. 2020). To investigate the effect of confinement
263 on our FCS measurements, we performed Brownian dynamics simulations of FCS experiments
264 with particles undergoing three-dimensional, purely Brownian diffusion inside a bacterial-cell like
265 volume (Figure 2A *Inset*; see Materials and Methods). For the values of cell diameter commonly
266 observed under our growth conditions, 0.8-0.9 μm, and over a wide range of particle diffusion
267 coefficients, simulated autocorrelation functions could be indeed successfully fitted with the
268 anomalous diffusion model, yielding an anomalous diffusion exponent of around 0.8-0.9 (Figure
269 2A and 2B). This made us hypothesize that the relatively small apparent deviation from Brownian
270 diffusion in the fit, common to most constructs, may primarily reflect a confinement-induced effect
271 rather than proper subdiffusion. In order to test this, we grew *E. coli* in presence of the inhibitor
272 A22, that is known to affect the biosynthesis of bacterial cell wall and lead to increased cell width
273 (Ouzounov et al. 2016). Indeed, the cell diameter (Figure 2C) and the anomalous diffusion
274 exponent of sfGFP (Figure 2D) both significantly increased upon such A22 treatment. We
275 conclude that the values of α above 0.8, as observed for most protein constructs, reflect Brownian
276 diffusion with confinement rather than truly anomalous diffusion.

277 We thus derived an Ornstein-Uhlenbeck (OU) model for fitting FCS data, where the confinement
278 of Brownian diffusing fluorescent particles within the width of the cell is approximated by trapping
279 in a harmonic potential of the same width (Appendix 2). The two models fit the ACF of the
280 Brownian dynamic simulations comparably well and better than the model of unconfined
281 Brownian diffusion (Figure 2A and Figure 2 - figure supplement 1), with the OU model having
282 one less free parameter than the anomalous diffusion model. The OU model directly estimates the
283 ansatz diffusion coefficient with ± 5% accuracy for the typical cell widths observed in our
284 experiments (Figure 2 – figure supplement 2).

285 We then applied the OU model to re-fit the ACF data for all faster diffusing constructs and to
286 estimate their Brownian diffusion coefficients. The OU proved accurate in fitting the experimental
287 data, comparably to the anomalous diffusion model (Figure 2 – figure supplement 3). The
288 dependence of D on molecular mass for this set of constructs was scaling as $(MM)^{-\beta}$ with $\beta = 0.56$
289 $\pm$ 0.05 (Figure 2E), less steep compared to the previous estimates (Kumar, Mommer, and Sourjik
290 2010; Mika et al. 2010; Stracy et al. 2021) but still steeper than expected from the Stokes-Einstein
291 relation, even when assuming $\beta = 0.4$ for not perfectly globular proteins (Figure 2E *Inset*) (Enright
292 and Leitner 2005; Smilgies and Folta-Stogniew 2015). In order to elucidate whether part of this
293 residual deviation may be accounted for by the specific shape of fusion constructs, where sfGFP
294 is fused to the differently-sized target proteins by a short flexible linker, we further applied a
295 previously derived model describing diffusion of such linked proteins (Appendix 3) (Agudo-
296 Canalejo and Golestanian 2020). The dependence of D on molecular mass predicted by this linked-
297 protein model seems indeed to better recapitulate our experimental data, particularly for smaller
298 protein fusions (Figure 2E *Inset*). Nevertheless, this model still clearly overestimates D for larger
299 protein fusions, suggesting that at least in this size range the dependence of D on molecular mass
300 in bacterial cytoplasm deviates from the Stokes-Einstein relation.

301

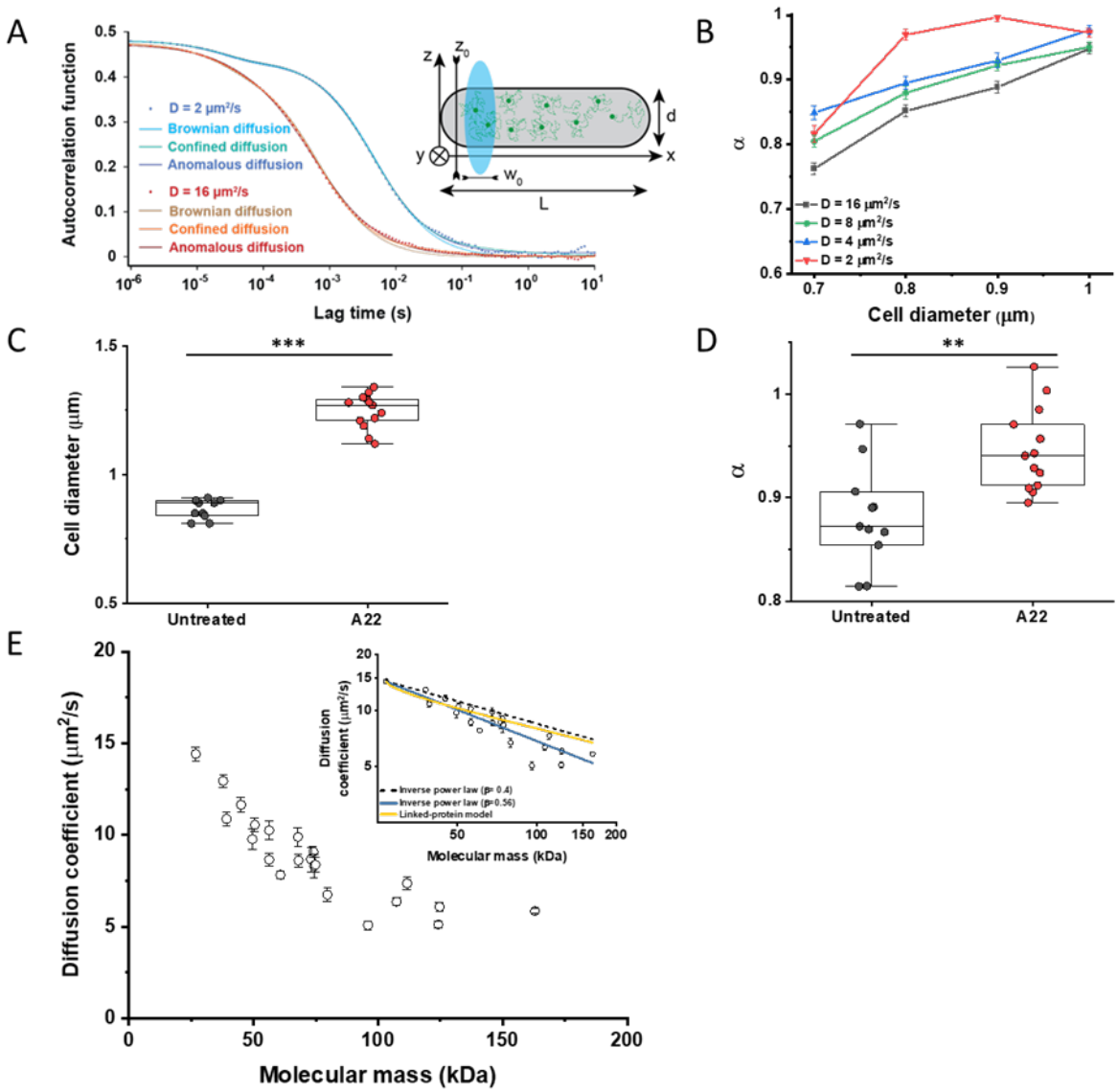

Figure 2. Protein diffusion in bacterial cytoplasm corrected for confinement. (A) Representative ACFs of simulated fluorescence intensity fluctuations. Simulations were performed in a confined geometry of a cell with indicated length L and diameter d, and dimensions of the measurement volume ω_0 and z_0, representing an experimental FCS measurement (*Inset*; see Materials and Methods) for two different values of the ansatz diffusion coefficient. Solid lines are fits by the models of unconfined Brownian diffusion, anomalous diffusion and by the Ornstein-Uhlenbeck (OU) model of Brownian diffusion under confinement, as indicated. (B) The exponent α extracted from the fit of the anomalous diffusion model to the ACFs data that were simulated at different values of the cell diameter. Corresponding values of the diffusion coefficient are shown in Figure 2 – figure supplement 2. (C,D) *E. coli* cells

311 grown for ~ 4 hours either in absence or in presence of 1 μg/mL of A22, show A22-dependent increase in the measured
312 cell diameter (C) and higher values of the exponent α extracted from the fit to the ACF measurements (D). For
313 consistency with other experiments, the cultures were also treated with cephalexin for 45 min. *** $p<0.0001$; * $p<0.05$
314 in a two-tailed heteroscedastistic *t*-test. (E) Dependence of the diffusion coefficient calculated from fitting the
315 experimental ACFs with the OU model of confined diffusion. Only the subset of apparently freely diffusing constructs
316 from Figure 1D has been analyzed with the OU model (see also Figure 1 – supplementary table 1). Each circle
317 represents the average value for all individual cells that have been measured for that particular construct, and the error
318 bars represent the standard error of the mean. *Inset* shows the fit of the mass dependence with an inverse power law
319 (solid blue line, exponent $\beta = 0.56 \pm 0.05$), and predictions of the Stokes-Einstein relation (black dashed line) and of
320 the model describing diffusion of two linked globular proteins (solid yellow line), both with exponent $\beta = 0.4$.

321 **Figure 2 – source data 1.** Original values used for plots in Figure 2B-E.

322

323 Protein diffusion coefficients measured using FRAP or FCS are consistent

324 Since many previous measurements of protein diffusion in bacteria were performed using FRAP,
325 we aimed to directly compare the results of FRAP and FCS measurements for a set of constructs
326 of different mass. Importantly, we used the same growth conditions and microscopy sample
327 preparation protocols as for the FCS experiments. The cells were photobleached in a region close
328 to the pole, similar to the position that was used for the FCS experiment. The recovery of
329 fluorescence was then followed for 11 seconds with the time resolution of 18 ms (Figure 3A). The
330 diffusion coefficients were computed from the time course of recovery with the plugin for ImageJ,
331 simFRAP (Blumenthal et al. 2015), which utilizes a simulation-based approach (Figure 3B). We
332 observed very good correlation between both values of diffusion coefficients, although for most
333 constructs the diffusion coefficients determined by FRAP were 5 to 30% lower than those obtained
334 from the FCS data (Figure 3C and Figure 1 – supplementary table 1).

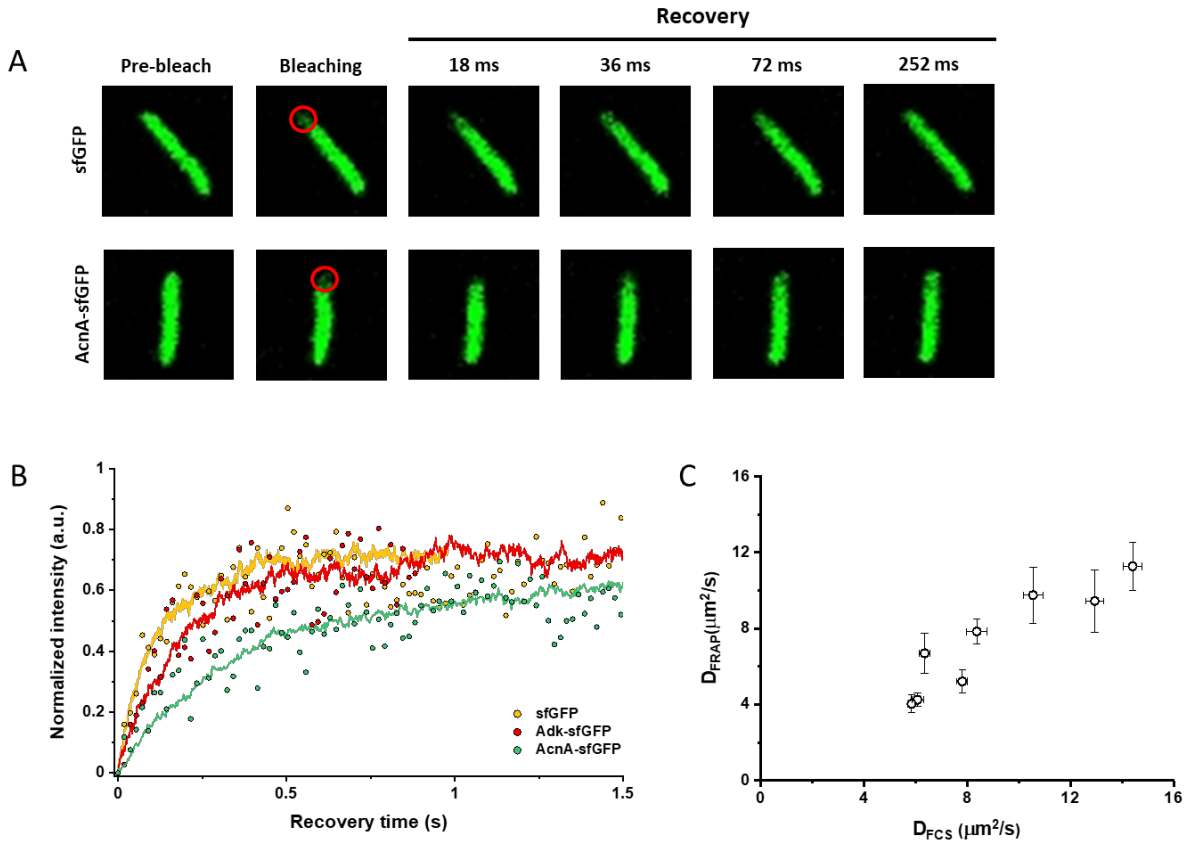

Figure 3. Comparison between protein diffusion coefficients measured by FCS and FRAP. (A) Examples of FRAP measurements for two different constructs, sfGFP and AcnA-sfGFP. A 3x3 pixels area close to one cell pole (red circle) was photobleached with a high intensity laser illumination for 48 ms and the recovery of fluorescence in the bleached area was monitored for 11 s with the time resolution of 18 ms. (B) Representative curves of fluorescence recovery in FRAP experiments and their fitting using simFRAP. The experimental data (colored dots) are used by the simFRAP algorithm to simulate the underlying diffusional process (colored lines). The simulation is then used to compute the diffusion coefficient. The simulation proceeds until the recovery curve reaches a plateau, therefore it is interrupted at a different time for each curve. (C) Correlation between the diffusion coefficients measured in FCS experiments (D_{FCS}, fitting with the OU model; data from Figure 2E) and in FRAP experiment (D_{FRAP}, fitting with simFRAP). Error bars represent the standard error of the mean.

Figure 3 – source data 1. Original values used for plot in Figure 3C.

348

349 **Effects of temperature, osmolarity and antibiotics on protein mobility**

350 Having established the assay of protein mobility, we selected several differently-sized constructs
351 with high mobility to characterize the impact of environmental and cellular perturbations that can
352 be experienced by bacterial cells. We first confirmed the previously well characterized (Konopka
353 et al. 2006; Konopka et al. 2009; Mika et al. 2010; Liu et al. 2019) decrease in protein mobility in
354 bacterial cytoplasm upon osmotic upshift. Exposing *E. coli* cells to increased ionic strength by
355 addition of 100 mM NaCl indeed decreased mobility of sfGFP by 30% (Figure 4 – figure
356 supplement 1), which is comparable to previously measured values (Konopka et al. 2009).

357 Next, we studied the effect of temperature on protein mobility in bacterial cytoplasm. According
358 to the Stokes-Einstein equation, the diffusion of a particle directly depends on the system's
359 temperature in Kelvin and on the viscosity of the fluid, which itself changes with temperature. In
360 the biologically relevant range, the temperature sensitivity of diffusion is primarily determined by
361 the temperature dependence of water viscosity. The measured increase in mobility of sfGFP and
362 two other constructs, by approximately 20-25% between 25°C and 35°C (Figure 4A), agrees well
363 with the expected temperature-dependent decrease in water viscosity over 10°C (Huber et al.
364 2009). Importantly, growth temperature of *E. coli* culture had no apparent effect on protein
365 mobility (Figure 4 – figure supplement 2), suggesting that – at least in the tested temperature range
366 – *E. coli* lacks the growth-temperature dependent regulation of cytoplasmic viscosity that has been
367 recently reported in the budding yeast (Persson, Ambati, and Brandman 2020).

368 Antibiotics that inhibit transcription (e.g., rifampicin) or translation (e.g., chloramphenicol) are
369 well known to affect the spatial organization of bacterial chromosomes (Bakshi et al. 2014), but

370 their effects on the diffusive properties of the cytoplasm are less established. We observed that
371 protein mobility significantly increased upon inhibition of RNA transcription by rifampicin
372 treatment, roughly independently of protein size (Figure 4B and Figure 4 – figure supplement 3).
373 In contrast, inhibition of protein translation by chloramphenicol slightly reduced mobility.

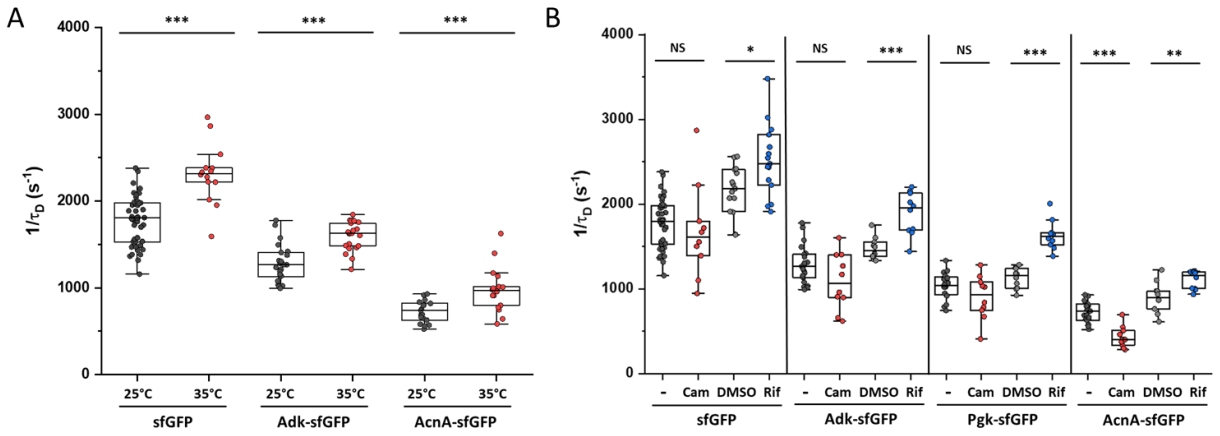

374

375 **Figure 4. Effects of temperature and antibiotics on protein mobility.** (A) The effect of environmental temperature
376 on mobility of indicated protein constructs. As for other experiments, *E. coli* culture was grown at 37°C. (B) The
377 effects of antibiotics treatment on mobility of indicated protein constructs. Chloramphenicol (Cam; 200 µg/mL),
378 rifampicin (Rif; 200 µg/mL, in 0.1% v/v DMSO), or DMSO control (0.1% v/v) were added to growing *E. coli* culture
379 60 minutes prior to harvesting. *** $p<0.0001$; ** $p<0.001$; * $p<0.05$; NS: no statistically significant difference in a
380 two-tailed heteroscedastistic *t*-test.

381 **Figure 4 – source data 1.** Original values used for plots in Figure 4.

382

383 ## Effects of cell growth on protein mobility

384 In order to further investigate whether protein mobility might be affected by cell growth, we
385 compared cells that were incubated at 35°C on agarose pads containing either only M9 salts or M9
386 salts plus glucose and casamino acids. The observed mobility was indeed significantly higher in

387 the presence of nutrients, and this increase was similar (~ 40%) for the two tested differently-sized

388 constructs (Figure 5).

389

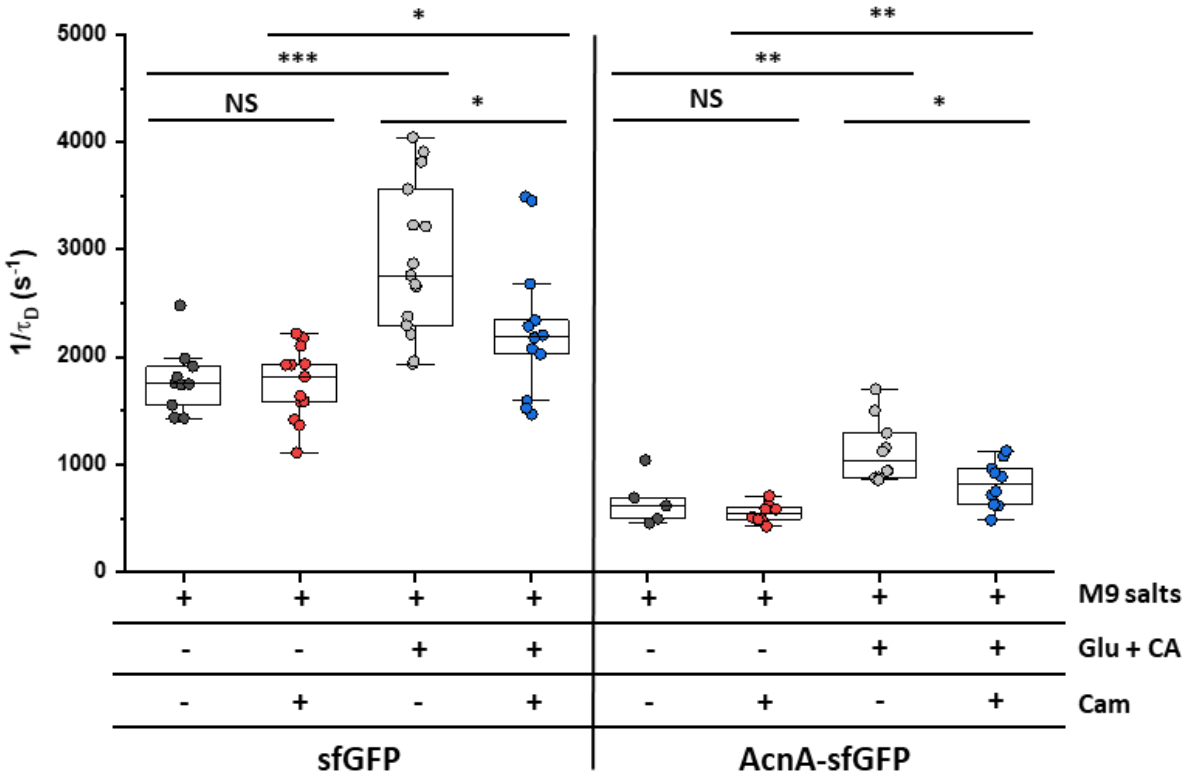

390

391 **Figure 5. Effect of nutrient availability and growth on protein mobility.** The mobility of indicated protein

392 constructs was measured in cells incubated at 35°C on agarose pads containing either only M9 salts or M9 salts

393 together with 20 mM glucose and 0.2% casamino acids (Glu + CA). Where indicated, chloramphenicol (Cam) was

394 also added to the agarose pads. *** $p<0.0001$; ** $p<0.001$; * $p<0.05$ in a two-tailed heteroscedastistic *t*-test.

395 **Figure 5 – source data 1.** Original values used for plots in Figure 5.

396

397 To distinguish the respective contributions of metabolic activity, and of biosynthesis and resulting

398 cell growth, we incubated cells in presence of both nutrients and chloramphenicol on the agarose

399 pad. Similar to our previous experiments where chloramphenicol was added to the batch culture,
400 its addition had no or little effect on protein mobility in absence of nutrients. In contrast, protein
401 mobility in presence of nutrients was strongly affected by chloramphenicol treatment. Thus, the
402 enhanced protein mobility in presence of nutrients largely depends on active protein production
403 and cell growth. Nevertheless, even chloramphenicol-treated cells exhibited a moderate increase
404 in protein mobility in presence of nutrients, indicating that the metabolic activity might also
405 contribute to the overall effect.

406

407 # Discussion

408 Bacteria rely on translational diffusion to deliver proteins and other macromolecules to their
409 cellular destinations, including their reaction partners, and the diffusional properties of bacterial
410 cytoplasm are therefore fundamental to the understanding of bacterial cell biology. Consequently,
411 a number of studies have investigated protein mobility in bacteria, all showing strong effects of
412 macromolecular crowding in the bacterial cytoplasm on diffusion (Konopka et al. 2006;
413 Mullineaux et al. 2006; Konopka et al. 2009; Kumar, Mommer, and Sourjik 2010; Mika et al.
414 2010; Nenninger, Mastroianni, and Mullineaux 2010). Nevertheless, the relatively small number
415 of proteins investigated in each of these previous studies, and the differences between strains,
416 growth conditions and, particularly, between methodologies, limited general conclusions about
417 protein mobility, even in the most-studied environment of *E. coli* cytoplasm. For example,
418 combining data from different studies to determine the relation between size of a protein and its
419 cytoplasmic diffusion coefficient yielded only uncertain estimates (Mika and Poolman 2011;
420 Schavemaker, Boersma, and Poolman 2018). Such variability between different studies might be

421 further compounded by potentially profound effects on diffusion of size-independent protein
422 properties such as surface charge (Schavemaker, Smigiel, and Poolman 2017). Similarly, it
423 remains unclear whether a typical protein in the cytoplasm exhibits Brownian diffusion, as has
424 been shown in few examples (Bakshi, Bratton, and Weisshaar 2011; English et al. 2011), or rather
425 a subdiffusive behavior as common for proteins in eukaryotic cells (Di Rienzo et al. 2014; Sabri
426 et al. 2020) and for bacterial mRNA-protein complexes (Lampo et al. 2017; Golding and Cox
427 2004), and what might be the possible causes of anomalous diffusion in bacteria.

428 Here, we addressed these questions by systematically investigating the diffusive behavior of a
429 large set of fluorescent protein fusions to differently-sized cytoplasmic proteins of *E. coli*. We
430 demonstrate that, despite their diverse cellular functions, the majority of studied proteins exhibit a
431 rather uniform relation between their molecular mass and cytoplasmic mobility, with a clear upper
432 bound on protein mobility at a given molecular mass. Furthermore, the apparent weak anomaly of
433 diffusion observed in the FCS data analysis, with $\alpha \sim 0.85$-0.9 for most proteins, could be
434 accounted for by confinement of the otherwise purely Brownian diffusing particles in the small
435 volume of a bacterial cell. Similar conclusions have been drawn by previous SPT studies for
436 several individual proteins (Bakshi, Bratton, and Weisshaar 2011; English et al. 2011). This
437 interpretation was directly confirmed by performing FCS measurements in *E. coli* with an
438 increased cell diameter, which indeed yielded $\alpha \sim 0.95$.

439 We therefore used a model of purely Brownian diffusion under confinement (Ornstein-Uhlenbeck
440 model) to determine diffusion coefficients by directly fitting the autocorrelation functions of our
441 FCS measurements. The obtained overall dependence of diffusion coefficients on the molecular
442 mass of the fusion protein showed the exponent $\beta = 0.56$, steeper than predicted by the Stokes-
443 Einstein relation, with $\beta = 0.33$ for fully compact proteins or $\beta = 0.4$ for the more realistic case

444 where proteins are assumed to be not entirely compact (Enright and Leitner 2005; Smilgies and
445 Folta-Stogniew 2015). Nevertheless, at least for smaller constructs, the observed dependence of
446 the diffusion coefficient on the molecular mass could be well reproduced when the specific shape
447 of fusion constructs, where two roughly globular proteins are fused by a short linker, was taken
448 into account along with their imperfect globularity (Agudo-Canalejo and Golestanian 2020). In
449 contrast, the diffusion of larger proteins was still slower than calculated by this model.

450 Our analysis thus suggests that, despite the high crowdedness of the bacterial cytoplasm, the
451 diffusion of typical cytoplasmic proteins in bacteria is mostly Brownian and can be well described
452 by treating the cytoplasm as a viscous fluid, with only a moderate dependence of the effective
453 viscosity on the size of diffusing proteins. Given the diffusion coefficient determined in our study
454 for free sfGFP, ~14 $\mu m^2 s^{-1}$, for small proteins this effective viscosity of bacterial cytoplasm is only
455 approximately six times higher than in dilute solution (Potma et al. 2001). This diffusion
456 coefficient for GFP is substantially larger than the values reported in the early studies that used
457 FRAP (Elowitz Michael et al. 1999; Konopka et al. 2006; Mullineaux et al. 2006; Konopka et al.
458 2009; Kumar, Mommer, and Sourjik 2010; Mika et al. 2010; Nenninger, Mastroianni, and
459 Mullineaux 2010), although it is consistent with other FCS and SPT studies (Meacci et al. 2006;
460 English et al. 2011; Sanamrad et al. 2014; Diepold et al. 2017; Rocha et al. 2019). These
461 differences are apparently due to the limitations of early FRAP analyses that generally
462 underestimated protein mobility, rather than due to different spatial and temporal scales assessed
463 by the two techniques, since our direct comparison between FCS and FRAP measurements yielded
464 similar values of diffusion coefficients. Indeed, a more recent FRAP study also reported higher
465 diffusion coefficients for GFP (Schavemaker, Smigiel, and Poolman 2017).

466 Several proteins in our set showed much lower mobility than expected from their size, and in some
467 cases also clearly subdiffusive behavior. For three selected examples, such deviation could be
468 explained by specific association of these proteins with other proteins or multiprotein complexes.
469 This is consistent with theoretical studies suggesting that binding of diffusing molecules to
470 crowders can lead to subdiffusion (Saxton 2007; Guigas and Weiss 2008). A similar explanation
471 is likely to hold for the other aberrantly slow proteins.

472 Unspecific transient interactions might also explain the slightly subdiffusive behavior of sfGFP
473 fusions to proteins from other bacteria in *E. coli* cytoplasm. However, this anomaly was weak and
474 there was overall only little difference between the mobility of these non-native proteins and their
475 similarly-sized *E. coli* homologues, in contrast to pronounced differences observed between
476 bacterial and mammalian proteins (Mu et al. 2017). Thus, there is apparently little organism-
477 specific adaptation of freely diffusing proteins to their "bacterial host", with a possible exception
478 of bacteria with very different pH or ionic strength of the cytoplasm (Schavemaker, Smigiel, and
479 Poolman 2017), which might facilitate horizontal gene transfer among bacteria.

480 We further probed how the effective viscous properties of bacterial cytoplasm changed under
481 different physicochemical perturbations, using a subset of proteins that showed fast diffusion for
482 their molecular mass as "reporters" of effective viscosity. Consistent with the importance of
483 macromolecular crowding and in agreement with previous results (Konopka et al. 2009), protein
484 mobility decreased upon osmotic upshift that increases cytoplasmic crowding. In contrast, the
485 effective cytoplasmic viscosity significantly (~20%) decreases upon treatment with rifampicin that
486 inhibits transcription and thereby reduces the overall macromolecular crowding. This observation
487 is consistent with recent SPT measurements (Wlodarski et al. 2017; Rotter et al. 2021), and it

488 agrees well with the relative contribution of RNA to the macromolecular composition of an *E. coli*
489 cell (Cayley et al. 1991).

490 Despite multiple effects of environmental temperature on cellular processes, temperature
491 dependence of the cytoplasmic viscosity in the tested range was similar to that of water and
492 consistent with the Stokes-Einstein relation, decreasing by 20-30% for a temperature increase of
493 10°C (Huber et al. 2009). We observed no dependence of the effective cytoplasmic viscosity on
494 growth temperature, in contrast to the homeostatic adaptation of bacterial membrane fluidity
495 (Sinensky 1974) and of bacterial signaling (Oleksiuk et al. 2011; Almblad et al. 2021) to the growth
496 temperature. Since growth-temperature dependent adaptation of the cytosolic viscosity was
497 recently reported for budding yeast (Persson, Ambati, and Brandman 2020), it is surprising that
498 such compensation apparently does not exist in *E. coli*. One possible explanation for this difference
499 might be a broader range of growth temperatures for budding yeast *Saccharomyces cerevisiae*
500 compared to *E. coli* and a stronger temperature effect on protein diffusion in the yeast cytosol. Of
501 note, here we did not explore protein diffusion in thermally stressed *E. coli* cells, which might have
502 more profound effects on the properties of bacterial cytoplasm as recently shown for *Listeria*
503 *monocytogenes* (Tran et al. 2021).

504 Finally, we observed that protein mobility was significantly higher in actively growing cells. This
505 "fluidizing" effect of growth seems to be primarily due to the biosynthetic processes, likely protein
506 translation, or to cell growth itself, whereas the effect of metabolic activity in presence of nutrients
507 was weaker although still significant. Thus, the observed phenomenon may be different from
508 previously characterized energy-dependent fluidization of the bacterial cytoplasm that enables
509 mobility of large multiprotein complexes but apparently does not affect free GFP (Montero Llopis

510 et al. 2012; Parry et al. 2014). The interplay between these energy-, metabolism- and growth-
511 dependent effects on diffusional properties of bacterial cytoplasm remains to be investigated.

512 Summarizing, here we present a comprehensive study of the diffusional properties of proteins in
513 the cytoplasm of *E. coli*, combining FCS measurements with theoretical modeling of diffusion in
514 a confined geometry of a bacterial cell. This analysis enabled us to distinguish a large set of
515 proteins with essentially Brownian diffusion, which could be used to characterize the effective
516 cytoplasmic viscosity over a range of molecular masses and its dependence on macromolecular
517 crowding, protein interactions, environmental temperature and cell growth.

518

519 Materials and methods

520 Bacterial strains, plasmids and media

521 All strains and plasmids used in this study are listed in Figure 1 – supplementary table 2. All
522 experiments were performed in the *Escherichia coli* strain W3110 (Serra et al. 2013). Genes of
523 interest were amplified by PCR using Q5 polymerase (New England Biosciences) and cloned
524 along with sfGFP using Gibson assembly (Gibson et al. 2009) into pTrc99A vector (Amann, Ochs,
525 and Abel 1988), under control of the *trc* promoter inducible by isopropyl ß-D-1-
526 thiogalactopyranoside (IPTG). In all cases sfGFP was fused at the C-terminus of the protein of
527 interest with a GGGGS linker. The stability of the fusion constructs was verified by gel
528 electrophoresis and immunoblotting using an anti-GFP primary antibody (JL-8 monoclonal,
529 Takara). Point mutations were introduced by site-directed mutagenesis (New England
530 Biosciences). *ΔclpA* was generated by transferring the kanamycin resistance cassette from the
531 corresponding mutant in the Keio collection (Baba et al. 2006) by P1 transduction. The cassette

532 was further removed by FLP recombinase carried on the temperature-sensitive plasmid pCP20
533 (Cherepanov and Wackernagel 1995).

534 *E. coli* cultures were grown in M9 minimal medium (48 mM Na_2HPO_4, 22 mM KH_2PO_4, 8.4 mM
535 NaCl, 18.6 mM NH_4Cl) supplemented with 0.2% casamino acids, 0.4% glucose and 100 µg/mL
536 ampicillin for selection. The overnight cultures were diluted to OD_{600} = 0.035 and grown for 3.5
537 hours at 37°C and 200 rpm shaking. Cultures were treated for additional 45 minutes, under the
538 same temperature and shaking conditions, with 10 µg/mL cephalexin and with 0 - 15 µM IPTG
539 (Figure 1 – supplementary table 1), to induce expression of the fluorescent protein constructs.
540 Where indicated, cultures were further incubated with 200 µg/mL rifampicin, 200 µg/mL
541 chloramphenicol or DMSO as a mock treatment for 1 hour under the same temperature and shaking
542 conditions.

543

544 FCS data acquisition

545 Cells were harvested by centrifugation at 7000g for 3 minutes and washed 3 times in tethering
546 buffer (10 mM K_2HPO_4, 10 mM KH_2PO_4, 1 µM methionine, 10 mM sodium lactate, buffered with
547 NaOH to pH 7). 2.5 µL of bacterial cells were then spread on a small 1% agarose pad prepared in
548 tethering buffer salts (10 mM K_2HPO_4, 10 mM KH_2PO_4 buffered with NaOH to pH 7), unless
549 differently stated. Imaging was performed on Ibidi 2-well µ-Slides (#1.5H, 170 µm ± 5 µm). After
550 the 45 minutes treatment with cephalexin, length of most bacterial cells was in a range of 4-8 µm.
551 For consistency, only cells of 5 ± 1 µm in length were selected for FCS experiments.

552 FCS measurements were performed on a LSM 880 confocal laser scanning microscope (Carl Zeiss
553 Microscopy) using a C-Apochromat 40×/1.2 water immersion objective selected for FCS. sfGFP

554 was excited with a 488 nm Argon laser (25 mW) and fluorescence emission was collected from
555 490 to 580 nm. Each sample was equilibrated for at least 20 minutes at 25°C (or 35°C when
556 specified), on the stage of the microscope and measurements were taken at the same temperature.
557 FCS measurements were acquired within 60 minutes from the sample preparation. The pinhole
558 was aligned on a daily basis, by maximizing the fluorescence intensity count rate of an Alexa488
559 (Invitrogen) solution (35 nM) in phosphate-buffered saline (PBS; 137 mM NaCl, 2.7 mM KCl, 8
560 mM Na_2HPO_4, 1.8 mM KH_2PO_4, pH 7.4). The coverslip collar adjustment ring of the water
561 immersion objective was also adjusted daily, maximizing the fluorescence intensity signal and the
562 brightness of Alexa 488. The laser power was adjusted in order to obtain molecular brightness (i.e.
563 photon counts per second per molecule, cpsm) of 10 kcpsm for Alexa 488, using the ZEN software
564 (Carl Zeiss Microscopy). The brightness of Alexa 488 was used as a daily reference to ensure
565 constant laser power and adjusting it using the software-provided laser power percentage whenever
566 necessary (range over the entire set of measurements was 0.11 – 0.18%). Before each measurement
567 session, we acquired three sequential FCS measurements of Alexa488 in PBS, to verify the
568 reproducibility of the confocal volume shape and size. The ratio between axial and lateral beam
569 waist $S = \frac{z_0}{\omega_0}$ = 8.0 ± 0.2 was obtained from a Brownian fit of the Alexa 488 autocorrelation
570 curves using the ZEN software. For the lateral beam waist, we obtained ω_0 = 0.186 ± 0.001 μm,
571 calculated from the diffusion time τ_D = 20.9 ± 0.11 μs obtained from the Brownian fit, being

572 $$D = \frac{\omega_0^2}{4\tau_D} \quad (1)$$

573 and being $D_{Alexa488}$ = 414 μm^2/s at 25°C (Petrov et al. 2006).

574 For the FCS measurements *in vivo*, the laser was positioned at the center of the short length axis
575 and typically 0.8-1 μm from one of the cell poles along the long axis. The positioning was chosen

576 to maintain distance from the cell membranes and to keep the confocal volume possibly away from
577 the bacterial chromosome. For each cell, six sequential fluorescence intensity acquisitions of 20
578 seconds each were performed on the same spot (Figure 1 – figure supplement 2). The laser power
579 used for measurements *in vivo* was fixed to a value about 7 times lower than for Alexa488 in PBS,
580 in order to reduce photobleaching. Confocal images of the selected cell were routinely acquired
581 before and after the FCS measurement to verify focal (*z*) and positioning (*xy*) stability (see
582 Appendix 1 for additional information on the FCS measurements).

583

584 **FCS data analysis**

585 Due to the small size of bacterial cells, fluorescence intensity traces are affected by photobleaching
586 (Appendix 1). The effect of photobleaching on autocorrelation curves was corrected by detrending
587 the long-time fluorescence decrease of each of the six fluorescence intensity traces using an ImageJ
588 plugin (Jay Unruh, https://research.stowers.org/imagejplugins/index.html, Stowers Institute for
589 Medical Research, USA). The plugin calculates the autocorrelation function (ACF) from each
590 fluorescence intensity trace, correcting it for the photobleaching effect by approximating the
591 decreasing fluorescence intensity trend with a multi-segment line (the number of segments was
592 fixed to two). We obtained almost identical ACFs correcting for photobleaching effects by local
593 averaging (Appendix 1 - figure 3) using the FCS-dedicated software package Fluctuation Analyzer
594 (Wachsmuth et al. 2015). In both cases, ACFs were calculated starting at 2 μs, since at times
595 shorter than 2 μsec, ACFs can be significantly affected by the GaAsp photomultipliers
596 afterpulsing.

597 For each FCS measurement, we fitted all the six ACFs, calculated using the multi-segment
598 detrending method, with a three-dimensional anomalous diffusion model that includes one
599 diffusive component and one blinking component due to the protonation-deprotonation of the
600 chromophore of sfGFP, according to the Equation (2):

601 $$G(\tau) = G_\infty + \frac{1}{N}\left(\frac{1-F_P+F_P e^{-\frac{\tau}{\tau_P}}}{1-F_P}\right)\frac{1}{1+\left(\frac{\tau}{\tau_D}\right)^\alpha\sqrt{1+\frac{1}{S^2}\left(\frac{\tau}{\tau_D}\right)^\alpha}} \quad (2)$$

602 where N is the average number of particles in the confocal volume, F_P is the fraction of particles
603 in the non-fluorescent state, τ_P is the protonation-deprotonation lifetime at pH 7.5, $S = \frac{z_0}{\omega_0}$, the
604 aspect ratio of the confocal volume with z_0 and ω_0 being the axial and lateral beam waists, τ_D is the
605 diffusion time in the confocal volume, α is the anomalous diffusion exponent, and G_∞ is the offset
606 of the autocorrelation function. The protonation-deprotonation lifetime (τ_P) for sfGFP was fixed
607 to 25 µs according to FCS measurements for sfGFP in PBS at pH 7.5 (Cotlet et al. 2006). The
608 aspect ratio of the confocal volume was fixed to S = 8 in the fittings to be consistent with the
609 experimental calibration (see above). All other parameters were left free. For each FCS
610 measurement, we calculated the average diffusion time τ_D and the average anomalous diffusion
611 exponent α based on the autocorrelation curves of the six sequential fluorescence intensity traces.
612 Importantly, no significant trend in τ_D or α was apparent when comparing the six sequential
613 autocorrelation functions acquired for a given bacterial cell (Appendix 1 - figure 4). Fitting to the
614 anomalous diffusion model was performed using the Levenberg-Marquardt algorithm in the FCS
615 analysis-dedicated software QuickFit 3.0 developed by Jan Wolfgang Krieger and Jörg Langowski
616 (Deutsches Krebsforschungszentrum, Heidelberg, https://github.com/jkriege2/QuickFit3). Identical
617 results were obtained when fitting the data with OriginPro.

618 Alternatively, the autocorrelation functions were fitted by the Ornstein-Uhlenbeck model
619 (Appendix 2) according to Equation (3):

620 $$G(\tau) = G_\infty + \frac{1}{N}\left(\frac{1-F_P+F_P e^{-\frac{\tau}{\tau_P}}}{1-F_P}\right)\left(1+2\frac{\sigma^2}{\omega_0^2}\frac{1-e^{-\frac{1\omega_0^2}{2\sigma^2}\frac{\tau}{\tau_D}}}{1+\frac{1\omega_0^2}{8\sigma^2}}\right)^{-\frac{1}{2}}\left(1+\frac{\tau}{\tau_D}\right)^{-\frac{1}{2}}\left(1+2\frac{\sigma^2}{S^2\omega_0^2}\frac{1-e^{-\frac{1\omega_0^2}{2\sigma^2}\frac{\tau}{\tau_D}}}{1+\frac{1S^2\omega_0^2}{8\ \sigma^2}}\right)^{-\frac{1}{2}}$$

621 (3)

622 where S and τ_P were fixed to the same values mentioned for equation (2), ω_0 was fixed to 0.19 and
623 σ was fixed to $d/2$=0.42 µm, being d the typical diameter of an *E. coli* cell (see Ornstein-Uhlenbeck
624 model validation paragraph). Fitting to the Ornstein-Uhlenbeck model was performed with
625 OriginPro.

626

627 **FRAP data acquisition and analysis**

628 Cells for FRAP experiments were grown and prepared for imaging following the same protocol as
629 for the FCS measurements. Due to the higher sensitivity of FCS at low fluorophore concentrations,
630 several fusion constructs required higher induction by IPTG (Figure 1 – supplementary table 1) to
631 obtain fluorescence intensity suitable for FRAP. The same LSM 880 confocal microscope,
632 including objective and light path was used for FRAP as for the FCS measurements. The bacterial
633 cell was imaged at 40×40 pixels with 30× zoom (pixel size 0.177 µm) with a pixel dwell time of
634 3.15 µs. First, 15 pre-bleaching frames were acquired at 2% laser power, subsequently the
635 photobleaching was performed on a 3×3 pixels area on one cell pole with 100% laser power for a
636 total of 48 ms and 584 post-bleaching frames were acquired to monitor the fluorescence recovery.
637 We observed that the mobile fraction for all constructs was >0.9. FRAP measurements were
638 analyzed using simFRAP (Blumenthal et al. 2015), an ImageJ plugin based on a simulation

639 approach implemented in a fast algorithm, which bypasses the need of using analytical models to
640 interpolate the data. The simFRAP algorithm simulates two-dimensional random walks in each
641 pixel, using the first image acquired after bleaching to define initial and boundary conditions, and
642 it resolves numerically the diffusion equation by iterative simulation. The frame time and pixel
643 size were fixed respectively to 0.018 s and 0.177 μm, and the target cell and the bleached region
644 were defined as ImageJ ROIs (regions of interest). Of note, we used the target cell itself as a
645 reference to compensate for the gradual bleaching during the measurement, as done previously
646 (Kumar, Mommer, and Sourjik 2010). This enabled us to achieve the highest possible temporal
647 resolution, by reducing the acquisition area to a single *E. coli* cell. The FRAP derived diffusion
648 coefficient D_{FRAP} was directly obtained as output of the plugin.

649

650 **Brownian dynamics simulations**

651 We performed Brownian dynamics simulations of uncorrelated point particles under confinement.
652 The N = 50 fluorescent particles performed a random walk with steps taken from a Gaussian
653 distribution of width $\sqrt{2D\Delta t}$, with D the free diffusion coefficient and $\Delta t = 10^{-6}\ s$ the simulation
654 step. Confinement was imposed by redrawing the random steps that moved out of the confinement
655 volume. Imposing elastic reflections on the walls yielded identical results. The confinement
656 volume was assumed to be a cylinder of diameter d and length (L-d) closed at both ends by
657 hemispheric caps of diameter d, idealizing the shape of *E. coli*. The cell length was fixed to L = 5
658 μm. The diameter was varied in the range d = [0.7, 1] μm. The collected fluorescence intensity
659 was computed at each time step assuming a Gaussian intensity profile of the laser beam, $I(t) =$
660 $\sum_{i=1}^{N} I_G(\boldsymbol{r}_i(t) - \boldsymbol{r}_0)$ with $\boldsymbol{r}_i(t)$ the position of particle i, $\boldsymbol{r}_0$ the center of the confocal volume and

$I_G(\boldsymbol{r} = (x, y, z)) = \exp\left(-2\left(\frac{x^2+y^2}{\omega_0^2} + \frac{z^2}{z_0^2}\right)\right)$, with $\omega_0 = 200$ nm and $z_0 = 800$ nm the lateral and axial widths of the confocal volume. The normalized intensity autocorrelation $C(dt) = \frac{\langle I(t+dt)I(t)\rangle}{\langle I(t+dt)\rangle\langle I(t)\rangle} - 1$ is computed for logarithmically spaced lag times dt, to reflect experimental practices. The center of the confocal volume was chosen in the center of the cell along the *y* and *z* axes and 1 µm away from the edge of the cell along the longitudinal *x* axis of the cell, similarly to experimental conditions. The intensity autocorrelation function was finally multiplied by an exponential decay, $\left(1 + 0.1 * \exp -\frac{dt}{\tau_H}\right)/1.1$ with $\tau_H = 25$ µs, to mimic the blinking component due to the protonation-deprotonation process of sfGFP, before fitting with the different models of diffusion. The code used for this simulation is available in GitHub (https://github.com/croelmiyn/Simulation_FCS_in_Bacteria) and via DOI: 10.5281/zenodo.5940484.

Validation of fitting by the Ornstein-Uhlenbeck model

We first estimated the relation between the width σ of the potential well and the diameter *d* of the bacteria by fitting the ACF of the Brownian simulations with the OU model, fixing all parameters except σ to their ansatz values. The best fit was obtained for $\sigma \simeq d/2$ over the whole range of tested parameters. To mimic the fit procedure of experimental data and evaluate the accuracy of the diffusion coefficient estimation by the OU model (Fig. 2C), we then fixed $\sigma = d/2$, and ω_0 and z_0 to their ansatz values, since they are measured independently in experiments, whereas the diffusion coefficient, number of particles *N* in the confocal volume, fraction of triplet excitation and background noise were taken as free parameters.

682

683 ## Acknowledgements

684 We thank Lotte Søgaard-Andersen, Martin Thanbichler, Knut Drescher and Andreas Diepold for
685 providing bacterial genomic DNA. This work was supported by the Max Planck Society.

686

687 ## Competing Interests

688 The authors declare no competing interests.

689

690 ## References

691 Agudo-Canalejo, Jaime, Tunrayo Adeleke-Larodo, Pierre Illien, and Ramin Golestanian. 2018.
692 'Enhanced Diffusion and Chemotaxis at the Nanoscale', *Accounts of Chemical Research*,
693 51: 2365-72.

694 Agudo-Canalejo, Jaime, and Ramin Golestanian. 2020. 'Diffusion and steady state distributions
695 of flexible chemotactic enzymes', *The European Physical Journal Special Topics*, 229:
696 2791-806.

697 Agudo-Canalejo, Jaime, Pierre Illien, and Ramin Golestanian. 2020. 'Cooperatively enhanced
698 reactivity and "stabilitaxis" of dissociating oligomeric proteins', *Proceedings of the*
699 *National Academy of Sciences*, 117: 11894.

700 Almblad, Henrik, Trevor E. Randall, Fanny Liu, Katherine Leblanc, Ryan A. Groves, Weerayuth
701 Kittichotirat, Geoffrey L. Winsor, Nicolas Fournier, Emily Au, Julie Groizeleau,
702 Jacquelyn D. Rich, Yuefei Lou, Elise Granton, Laura K. Jennings, Larissa A. Singletary,
703 Tara M. L. Winstone, Nathan M. Good, Roger E. Bumgarner, Michael F. Hynes, Manu
704 Singh, Maria Silvina Stietz, Fiona S. L. Brinkman, Ayush Kumar, Ann Karen Cornelia

705 Brassinga, Matthew R. Parsek, Boo Shan Tseng, Ian A. Lewis, Bryan G. Yipp, Justin L.
706 MacCallum, and Joe Jonathan Harrison. 2021. 'Bacterial cyclic diguanylate signaling
707 networks sense temperature', *Nature Communications*, 12: 1986.

708 Amann, E., B. Ochs, and K. J. Abel. 1988. 'Tightly regulated tac promoter vectors useful for the
709 expression of unfused and fused proteins in *Escherichia coli*', *Gene*, 69: 301-15.

710 Baba, T., T. Ara, M. Hasegawa, Y. Takai, Y. Okumura, M. Baba, K. A. Datsenko, M. Tomita, B.
711 L. Wanner, and H. Mori. 2006. 'Construction of *Escherichia coli* K-12 in-frame, single-
712 gene knockout mutants: the Keio collection', *Molecular Systems Biology*, 2: 2006 0008.

713 Bakshi, Somenath, Benjamin P Bratton, and James C Weisshaar. 2011. 'Subdiffraction-Limit
714 Study of Kaede Diffusion and Spatial Distribution in Live *Escherichia coli*', *Biophysical*
715 *Journal*, 101: 2535-44.

716 Bakshi, Somenath, Heejun Choi, Jagannath Mondal, and James C. Weisshaar. 2014. 'Time-
717 dependent effects of transcription- and translation-halting drugs on the spatial
718 distributions of the *Escherichia coli* chromosome and ribosomes', *Molecular*
719 *Microbiology*, 94: 871-87.

720 Balbo, Jessica, Paolo Mereghetti, Dirk-Peter Herten, and Rebecca C. Wade. 2013. 'The shape of
721 protein crowders is a major determinant of protein diffusion', *Biophysical Journal*, 104:
722 1576-84.

723 Banks, Daniel S., and Cécile Fradin. 2005. 'Anomalous Diffusion of Proteins Due to Molecular
724 Crowding', *Biophysical Journal*, 89: 2960-71.

725 Blumenthal, D., L. Goldstien, M. Edidin, and L. A. Gheber. 2015. 'Universal Approach to FRAP
726 Analysis of Arbitrary Bleaching Patterns', *Scientific Reports*, 5: 11655.

727 Cayley, Scott, Barbara A. Lewis, Harry J. Guttman, and M. Thomas Record. 1991.
728 'Characterization of the cytoplasm of *Escherichia coli* K-12 as a function of external
729 osmolarity: Implications for protein-DNA interactions in vivo', *Journal of Molecular*
730 *Biology*, 222: 281-300.

731 Cherepanov, Peter P., and Wilfried Wackernagel. 1995. 'Gene disruption in *Escherichia coli*:
732 TcR and KmR cassettes with the option of Flp-catalyzed excision of the antibiotic-
733 resistance determinant', *Gene*, 158: 9-14.

734 Cluzel, Philippe, Michael Surette, and Stanislas Leibler. 2000. 'An Ultrasensitive Bacterial
735 Motor Revealed by Monitoring Signaling Proteins in Single Cells', *Science*, 287: 1652-
736 55.

737 Cotlet, M., P. M. Goodwin, G. S. Waldo, and J. H. Werner. 2006. 'A comparison of the
738 fluorescence dynamics of single molecules of a green fluorescent protein: one- versus
739 two-photon excitation', *Chemphyschem*, 7: 250-60.

740 Di Rienzo, Carmine, Vincenzo Piazza, Enrico Gratton, Fabio Beltram, and Francesco Cardarelli.
741 2014. 'Probing short-range protein Brownian motion in the cytoplasm of living cells',
742 *Nature Communications*, 5: 5891.

743 Diepold, A., E. Sezgin, M. Huseyin, T. Mortimer, C. Eggeling, and J. P. Armitage. 2017. 'A
744 dynamic and adaptive network of cytosolic interactions governs protein export by the
745 T3SS injectisome', *Nature Communications*, 8: 15940.

746 Dix, James A., and A. S. Verkman. 2008. 'Crowding Effects on Diffusion in Solutions and Cells',
747 *Annual Review of Biophysics*, 37: 247-63.

748 Einstein, Albert 1906. 'On the theory of the Brownian movement', *Annalen der Physik*, 19: 371-
749 81.

750 Elowitz Michael, B., G. Surette Michael, Pierre-Etienne Wolf, B. Stock Jeffry, and Stanislas
751 Leibler. 1999. 'Protein Mobility in the Cytoplasm of *Escherichia coli*', *Journal of*
752 *Bacteriology*, 181: 197-203.

753 Elson, E. L. 2011. 'Fluorescence correlation spectroscopy: past, present, future', *Biophysical*
754 *Journal*, 101: 2855-70.

755 Enderlein, Jörg. 2012. 'Polymer Dynamics, Fluorescence Correlation Spectroscopy, and the
756 Limits of Optical Resolution', *Physical Review Letters*, 108: 108101.

757 Enderlein, Jörg, Ingo Gregor, Digambara Patra, Thomas Dertinger, and U. Benjamin Kaupp.
758 2005. 'Performance of Fluorescence Correlation Spectroscopy for Measuring Diffusion
759 and Concentration', *Chemphyschem*, 6: 2324-36.

760 English, Brian P., Vasili Hauryliuk, Arash Sanamrad, Stoyan Tankov, Nynke H. Dekker, and
761 Johan Elf. 2011. 'Single-molecule investigations of the stringent response machinery in
762 living bacterial cells', *Proceedings of the National Academy of Sciences of the United*
763 *States of America*, 108: E365-E73.

764 Enright, Matthew B., and David M. Leitner. 2005. 'Mass fractal dimension and the compactness
765 of proteins', *Physical Review E*, 71: 011912.

766 Etoc, Fred, Elie Balloul, Chiara Vicario, Davide Normanno, Domenik Liße, Assa Sittner, Jacob
767 Piehler, Maxime Dahan, and Mathieu Coppey. 2018. 'Non-specific interactions govern
768 cytosolic diffusion of nanosized objects in mammalian cells', *Nature Materials*, 17: 740-
769 46.

770 Genevaux, P., C. Georgopoulos, and W. L. Kelley. 2007. 'The Hsp70 chaperone machines of
771 *Escherichia coli*: a paradigm for the repartition of chaperone functions', *Molecular*
772 *Microbiology*, 66: 840-57.

773 Gennerich, Arne, and Detlev Schild. 2000. 'Fluorescence Correlation Spectroscopy in Small
774 Cytosolic Compartments Depends Critically on the Diffusion Model Used', *Biophysical*
775 *Journal*, 79: 3294-306.

776 Gibson, D. G., L. Young, R. Y. Chuang, J. C. Venter, C. A. Hutchison, 3rd, and H. O. Smith.
777 2009. 'Enzymatic assembly of DNA molecules up to several hundred kilobases', *Nature*
778 *Methods*, 6: 343-5.

779 Goins, Aron B., Hugo Sanabria, and M. Neal Waxham. 2008. 'Macromolecular crowding and
780 size effects on probe microviscosity', *Biophysical Journal*, 95: 5362-73.

781 Golding, Ido, and Edward C. Cox. 2004. 'RNA dynamics in live *Escherichia coli* cells',
782 *Proceedings of the National Academy of Sciences of the United States of America*, 101:
783 11310.

784 Golestanian, Ramin. 2015. 'Enhanced Diffusion of Enzymes that Catalyze Exothermic
785 Reactions', *Physical Review Letters*, 115: 108102.

786 Guigas, Gernot, and Matthias Weiss. 2008. 'Sampling the Cell with Anomalous Diffusion—The
787 Discovery of Slowness', *Biophysical Journal*, 94: 90-94.

788 Huber, M. L., R. A. Perkins, A. Laesecke, D. G. Friend, J. V. Sengers, M. J. Assael, I. N.
789 Metaxa, E. Vogel, R. Mareš, and K. Miyagawa. 2009. 'New International Formulation for
790 the Viscosity of H2O', *Journal of Physical and Chemical Reference Data*, 38: 101-25.

791 Humbard, M. A., S. Surkov, G. M. De Donatis, L. M. Jenkins, and M. R. Maurizi. 2013. 'The N-
792 degradome of *Escherichia coli*: limited proteolysis in vivo generates a large pool of
793 proteins bearing N-degrons', *The Journal of Biological Chemistry*, 288: 28913-24.

794 Jiang, Yanfei, Bingxian Xu, Artem Melnykov, Guy M. Genin, and Elliot L. Elson. 2020.
795 'Fluorescence Correlation Spectroscopy and Photon Counting Histograms in Finite,
796 Bounded Domains', *Biophysical Journal*, 119: 265-73.

797 Joyner, Ryan P., Jeffrey H. Tang, Jonne Helenius, Elisa Dultz, Christiane Brune, Liam J. Holt,
798 Sebastien Huet, Daniel J. Müller, and Karsten Weis. 2016. 'A glucose-starvation response
799 regulates the diffusion of macromolecules', *Elife*, 5: e09376.

800 Kalwarczyk, Tomasz, Marcin Tabaka, and Robert Holyst. 2012. 'Biologistics--diffusion
801 coefficients for complete proteome of *Escherichia coli*', *Bioinformatics (Oxford,*
802 *England)*, 28: 2971-78.

803 Kapanidis, A. N., S. Uphoff, and M. Stracy. 2018. 'Understanding Protein Mobility in Bacteria
804 by Tracking Single Molecules', *Journal of Molecular Biology*, 430: 4443-55.

805 Klumpp, Stefan, Matthew Scott, Steen Pedersen, and Terence Hwa. 2013. 'Molecular crowding
806 limits translation and cell growth', *Proceedings of the National Academy of Sciences*,
807 110: 16754.

808 Konopka, M. C., I. A. Shkel, S. Cayley, M. T. Record, and J. C. Weisshaar. 2006. 'Crowding and
809 confinement effects on protein diffusion in vivo', *Journal of Bacteriology*, 188: 6115-23.

810 Konopka, M. C., K. A. Sochacki, B. P. Bratton, I. A. Shkel, M. T. Record, and J. C. Weisshaar.
811 2009. 'Cytoplasmic protein mobility in osmotically stressed *Escherichia coli*', *Journal of*
812 *Bacteriology*, 191: 231-7.

813 Kumar, M., M. S. Mommer, and V. Sourjik. 2010. 'Mobility of cytoplasmic, membrane, and
814 DNA-binding proteins in *Escherichia coli*', *Biophysical Journal*, 98: 552-9.

815 Kumar, Mohit, and Victor Sourjik. 2012. 'Physical map and dynamics of the chaperone network
816 in *Escherichia coli*', *Molecular Microbiology*, 84: 736-47.

817 Lampo, Thomas J., Stella Stylianidou, Mikael P. Backlund, Paul A. Wiggins, and Andrew J.
818 Spakowitz. 2017. 'Cytoplasmic RNA-Protein Particles Exhibit Non-Gaussian
819 Subdiffusive Behavior', *Biophysical Journal*, 112: 532-42.

820 Langevin, Paul. 1908. 'Sur la théorie du mouvement brownien', *Comptes-rendus de l'Académie*
821 *des sciences*, 146: 530-33.

822 Liu, B., Z. Hasrat, B. Poolman, and A. J. Boersma. 2019. 'Decreased Effective Macromolecular
823 Crowding in *Escherichia coli* Adapted to Hyperosmotic Stress', *Journal of Bacteriology*,
824 201.

825 Loren, N., J. Hagman, J. K. Jonasson, H. Deschout, D. Bernin, F. Cella-Zanacchi, A. Diaspro, J.
826 G. McNally, M. Ameloot, N. Smisdom, M. Nyden, A. M. Hermansson, M. Rudemo, and
827 K. Braeckmans. 2015. 'Fluorescence recovery after photobleaching in material and life
828 sciences: putting theory into practice', *Quarterly Reviews of Biophysics*, 48: 323-87.

829 Luby-Phelps, Katherine. 1999. 'Cytoarchitecture and Physical Properties of Cytoplasm: Volume,
830 Viscosity, Diffusion, Intracellular Surface Area.' in Harry Walter, Donald E. Brooks and
831 Paul A. Srere (eds.), *International Review of Cytology* (Academic Press).

832 Macháň, Radek, Yong Hwee Foo, and Thorsten Wohland. 2016. 'On the Equivalence of FCS and
833 FRAP: Simultaneous Lipid Membrane Measurements', *Biophysical Journal*, 111: 152-61.

834 Mayer, Matthias P., Stefan Rüdiger, and Bernd Bukau. 2000. 'Molecular Basis for Interactions of
835 the DnaK Chaperone with Substrates', *Biological Chemistry*, 381: 877-85.

836 Meacci, G., J. Ries, E. Fischer-Friedrich, N. Kahya, P. Schwille, and K. Kruse. 2006. 'Mobility
837 of Min-proteins in *Escherichia coli* measured by fluorescence correlation spectroscopy',
838 *Physical Biology*, 3: 255-63.

839 Mika, J. T., G. van den Bogaart, L. Veenhoff, V. Krasnikov, and B. Poolman. 2010. 'Molecular
840 sieving properties of the cytoplasm of *Escherichia coli* and consequences of osmotic
841 stress', *Molecular Microbiology*, 77: 200-7.

842 Mika, Jacek T., and Bert Poolman. 2011. 'Macromolecule diffusion and confinement in
843 prokaryotic cells', *Current Opinion in Biotechnology*, 22: 117-26.

844 Montero Llopis, Paula, Oleksii Sliusarenko, Jennifer Heinritz, and Christine Jacobs-Wagner.
845 2012. '*In vivo* biochemistry in bacterial cells using FRAP: insight into the translation
846 cycle', *Biophysical Journal*, 103: 1848-59.

847 Mu, Xin, Seongil Choi, Lisa Lang, David Mowray, Nikolay V. Dokholyan, Jens Danielsson, and
848 Mikael Oliveberg. 2017. 'Physicochemical code for quinary protein interactions in
849 *Escherichia coli*', *Proceedings of the National Academy of Sciences*, 114: E4556.

850 Mullineaux, C. W., A. Nenninger, N. Ray, and C. Robinson. 2006. 'Diffusion of green
851 fluorescent protein in three cell environments in *Escherichia coli*', *Journal of*
852 *Bacteriology*, 188: 3442-8.

853 Muramatsu, N., and A. P. Minton. 1988. 'Tracer diffusion of globular proteins in concentrated
854 protein solutions', *Proceedings of the National Academy of Sciences of the United States*
855 *of America*, 85: 2984-88.

856 Nenninger, A., G. Mastroianni, and C. W. Mullineaux. 2010. 'Size dependence of protein
857 diffusion in the cytoplasm of *Escherichia coli*', *Journal of Bacteriology*, 192: 4535-40.

858 Oleksiuk, O., V. Jakovljevic, N. Vladimirov, R. Carvalho, E. Paster, W. S. Ryu, Y. Meir, N. S.
859 Wingreen, M. Kollmann, and V. Sourjik. 2011. 'Thermal robustness of signaling in
860 bacterial chemotaxis', *Cell*, 145: 312-21.

861 Ouzounov, N., J. P. Nguyen, B. P. Bratton, D. Jacobowitz, Z. Gitai, and J. W. Shaevitz. 2016.
862 'MreB Orientation Correlates with Cell Diameter in *Escherichia coli*', *Biophysical*
863 *Journal*, 111: 1035-43.

864 Parry, B. R., I. V. Surovtsev, M. T. Cabeen, C. S. O'Hern, E. R. Dufresne, and C. Jacobs-
865 Wagner. 2014. 'The bacterial cytoplasm has glass-like properties and is fluidized by
866 metabolic activity', *Cell*, 156: 183-94.

867 Pédelacq, Jean-Denis, Stéphanie Cabantous, Timothy Tran, Thomas C. Terwilliger, and Geoffrey
868 S. Waldo. 2006. 'Engineering and characterization of a superfolder green fluorescent
869 protein', *Nature Biotechnology*, 24: 79-88.

870 Perrin, Jean. 1909. 'Mouvement brownien et réalité moléculaire', *Annales de chimie et de*
871 *physique*.

872 Persson, Laura B., Vardhaan S. Ambati, and Onn Brandman. 2020. 'Cellular Control of Viscosity
873 Counters Changes in Temperature and Energy Availability', *Cell*, 183: 1572-85.e16.

874 Petrov, E. P., T. Ohrt, R. G. Winkler, and P. Schwille. 2006. 'Diffusion and segmental dynamics
875 of double-stranded DNA', *Physical Review Letters*, 97: 258101.

876 Potma, Eric O., Wim P. de Boeij, Leonard Bosgraaf, Jeroen Roelofs, Peter J. M. van Haastert,
877 and Douwe A. Wiersma. 2001. 'Reduced Protein Diffusion Rate by Cytoskeleton in
878 Vegetative and Polarized Dictyostelium Cells', *Biophysical Journal*, 81: 2010-19.

879 Rivas, Germán, and Allen P. Minton. 2016. 'Macromolecular Crowding *In Vitro*, *In Vivo*, and In
880 Between', *Trends in Biochemical Sciences*, 41: 970-81.

881 Rocha, J., J. Corbitt, T. Yan, C. Richardson, and A. Gahlmann. 2019. 'Resolving Cytosolic
882 Diffusive States in Bacteria by Single-Molecule Tracking', *Biophysical Journal*, 116:
883 1970-83.

884 Roman-Hernandez, G., J. Y. Hou, R. A. Grant, R. T. Sauer, and T. A. Baker. 2011. 'The ClpS
885 adaptor mediates staged delivery of N-end rule substrates to the AAA+ ClpAP protease',
886 *Molecular Cell*, 43: 217-28.

887 Rotter, D. A. O., C. Heger, L. M. Oviedo-Bocanegra, and P. L. Graumann. 2021. 'Transcription-
888 dependent confined diffusion of enzymes within subcellular spaces of the bacterial
889 cytoplasm', *BMC Biology*, 19: 183.

890 Sabri, Adal, Xinran Xu, Diego Krapf, and Matthias Weiss. 2020. 'Elucidating the Origin of
891 Heterogeneous Anomalous Diffusion in the Cytoplasm of Mammalian Cells', *Physical*
892 *Review Letters*, 125: 058101.

893 Sanamrad, A., F. Persson, E. G. Lundius, D. Fange, A. H. Gynna, and J. Elf. 2014. 'Single-
894 particle tracking reveals that free ribosomal subunits are not excluded from the
895 *Escherichia coli* nucleoid', *Proceedings of the National Academy of Sciences of the*
896 *United States of America*, 111: 11413-8.

897 Sandikci, A., F. Gloge, M. Martinez, M. P. Mayer, R. Wade, B. Bukau, and G. Kramer. 2013.
898 'Dynamic enzyme docking to the ribosome coordinates N-terminal processing with
899 polypeptide folding', *Nature Structural & Molecular Biology*, 20: 843-50.

900 Saxton, M. J. 1996. 'Anomalous diffusion due to binding: a Monte Carlo study', *Biophysical*
901 *Journal*, 70: 1250-62.

902 Saxton, Michael J. 2007. 'A Biological Interpretation of Transient Anomalous Subdiffusion. I.
903 Qualitative Model', *Biophysical Journal*, 92: 1178-91.

904 Schavemaker, P. E., W. M. Smigiel, and B. Poolman. 2017. 'Ribosome surface properties may
905 impose limits on the nature of the cytoplasmic proteome', *Elife*, 6.

906 Schavemaker, Paul E., Arnold J. Boersma, and Bert Poolman. 2018. 'How Important Is Protein
907 Diffusion in Prokaryotes?', *Frontiers in Molecular Biosciences*, 5: 93.

908 Schwartz, Russell, Claire S. Ting, and Jonathan King. 2001. 'Whole Proteome pI Values
909 Correlate with Subcellular Localizations of Proteins for Organisms within the Three
910 Domains of Life', *Genome Research*, 11: 703-09.

911 Serra, D. O., A. M. Richter, G. Klauck, F. Mika, and R. Hengge. 2013. 'Microanatomy at cellular
912 resolution and spatial order of physiological differentiation in a bacterial biofilm', *mBio*,
913 4: e00103-13.

914 Sinensky, M. 1974. 'Homeoviscous adaptation--a homeostatic process that regulates the viscosity
915 of membrane lipids in *Escherichia coli*', *Proceedings of the National Academy of*
916 *Sciences of the United States of America*, 71: 522-25.

917 Smilgies, Detlef- M., and Ewa Folta-Stogniew. 2015. 'Molecular weight-gyration radius relation
918 of globular proteins: a comparison of light scattering, small-angle X-ray scattering and
919 structure-based data', *Journal of applied crystallography*, 48: 1604-06.

920 Solbiati, José, Anne Chapman-Smith, Judith L. Miller, Charles G. Miller, and John E. Cronan.
921 1999. 'Processing of the N termini of nascent polypeptide chains requires deformylation
922 prior to methionine removal', *Journal of Molecular Biology*, 290: 607-14.

923 Spitzer, Jan, and Bert Poolman. 2013. 'How crowded is the prokaryotic cytoplasm?', *FEBS*
924 *Letters*, 587: 2094-98.

925 Stasevich, Timothy J., Florian Mueller, Ariel Michelman-Ribeiro, Tilman Rosales, Jay R.
926 Knutson, and James G. McNally. 2010. 'Cross-validating FRAP and FCS to quantify the
927 impact of photobleaching on in vivo binding estimates', *Biophysical Journal*, 99: 3093-
928 101.

929 Stracy, M., J. Schweizer, D. J. Sherratt, A. N. Kapanidis, S. Uphoff, and C. Lesterlin. 2021.
930 'Transient non-specific DNA binding dominates the target search of bacterial DNA-
931 binding proteins', *Molecular Cell*, 81: 1499-514 e6.

932 Swaminathan, R., C. P. Hoang, and A. S. Verkman. 1997. 'Photobleaching recovery and
933 anisotropy decay of green fluorescent protein GFP-S65T in solution and cells:
934 cytoplasmic viscosity probed by green fluorescent protein translational and rotational
935 diffusion', *Biophysical Journal*, 72: 1900-07.

936 Tabaka, Marcin, Tomasz Kalwarczyk, Jedrzej Szymanski, Sen Hou, and Robert Holyst. 2014.
937 'The effect of macromolecular crowding on mobility of biomolecules, association
938 kinetics, and gene expression in living cells', *Frontiers in Physics*, 2.

939 Tran, Buu Minh, Haritha Prabha, Aditya Iyer, Conor O'Byrne, Tjakko Abee, and Bert Poolman.
940 2021. 'Measurement of Protein Mobility in *Listeria monocytogenes* Reveals a Unique
941 Tolerance to Osmotic Stress and Temperature Dependence of Diffusion', *Frontiers in*
942 *Microbiology*, 12.

943 Tyn, Myo T., and Todd W. Gusek. 1990. 'Prediction of diffusion coefficients of proteins',
944 *Biotechnology and Bioengineering*, 35: 327-38.

945 van den Berg, Jonas, Arnold J. Boersma, and Bert Poolman. 2017. 'Microorganisms maintain
946 crowding homeostasis', *Nature Reviews Microbiology*, 15: 309-18.

947 Wachsmuth, M., C. Conrad, J. Bulkescher, B. Koch, R. Mahen, M. Isokane, R. Pepperkok, and J.
948 Ellenberg. 2015. 'High-throughput fluorescence correlation spectroscopy enables analysis
949 of proteome dynamics in living cells', *Nature Biotechnology*, 33: 384-9.

950 Wlodarski, Michal, Bianca Raciti, Jurij Kotar, Marco Cosentino Lagomarsino, Gillian M. Fraser,
951 and Pietro Cicuta. 2017. 'Both genome and cytosol dynamics change in *E. coli* challenged
952 with sublethal rifampicin', *Physical Biology*, 14: 015005.

953 Zhang, Yifei, and Henry Hess. 2019. 'Enhanced Diffusion of Catalytically Active Enzymes', *ACS*
954 *Central Science*, 5: 939-48.

955 Zimmerman, Steven B., and Stefan O. Trach. 1991. 'Estimation of macromolecule concentrations
956 and excluded volume effects for the cytoplasm of *Escherichia coli*', *Journal of Molecular*
957 *Biology*, 222: 599-620.

958

959 # Supplementary files

960 This article contains the following supplementary files:

961 Figure 1 – supplementary table 1

962 Figure 1 – supplementary table 2

963 Figure 1 – figure supplement 1

964 Figure 1 – figure supplement 2

965 Figure 1 – figure supplement 3

966 Figure 1 – figure supplement 4

967 Figure 1 – figure supplement 5

968 Figure 1 – figure supplement 6

969 Figure 1 – figure supplement 7

970 Figure 2 – figure supplement 1

971 Figure 2 – figure supplement 2

972 Figure 2 – figure supplement 3

973 Figure 4 – figure supplement 1

974 Figure 4 – figure supplement 2

975 Figure 4 – figure supplement 3

976 Appendix 1: Notes on the acquisition and analysis protocols for FCS measurements in bacterial
977 cells

978 Appendix 2: Ornstein-Uhlenbeck model for confinement effect in FCS measurements

979 Appendix 3: Effective diffusion coefficient of two linked proteins

980 Appendix 4: Exact p-values for each figure

981 Appendix 5: Numerosity of the constructs and conditions for each experiment

982 Source data: Source data files and raw immunoblot images.

Supplementary figures

Figure 1 – supplementary table 1. sfGFP-tagged library of cytoplasmic proteins

Protein name	Molecular mass of sfGFP-construct	Biological function	IPTG concentration for FCS (for FRAP)	Number of cells (FCS)	τ_D (µs; avg. ± SE)	α (Avg. ± SE)	Diffusion coefficient, FCS (µm²/s, Avg. ± SE)	Number of cells (FRAP)	Diffusion coefficient, FRAP (µm²/s, Avg. ± SE)
sfGFP	26.9	-	5 µM (15 µM)	42	580 ± 15	0.86 ± 0.01	14.4 ± 0.4	11	11.3 ± 1.3
YggX	39.2	Probable Fe (2+)-trafficking protein	5 µM (5 µM)	8	611 ± 19	0.85 ± 0.01	12.9 ± 0.4	10	9.4 ± 1.6
ClpS	39.2	ATP-dependent Clp protease adapter protein	0 µM	11	1054 ± 33	0.75 ± 0.01			
FolK	45.1	2-amino-4-hydroxy-6-hydroxymethyldihydropteridine pyrophosphokinase	0 µM	8	734 ± 24	0.87 ± 0.01	11.6 ± 0.4		
Crr	45.2	Component of glucose-specific phosphotransferase enzyme IIA	0 µM	14	1065 ± 36	0.87 ± 0.01			
UbiC	45.7	Chorismate pyruvate-lyase	15 µM	14	1140 ± 58	0.87 ± 0.01			
ThpR	46.9	RNA 2',3'-cyclic phosphodiesterase	Discarded due to instability of sfGFP-construct						
CoaE	49.6	Dephospho-CoA kinase	0 µM	11	854 ± 47	0.87 ± 0.01	9.8 ± 0.6		
Adk	50.6	Adenylate kinase	5 µM (15 µM)	23	802 ± 26	0.88 ± 0.00	10.6 ± 0.4	16	9.8 ± 1.5
Cmk	51.7	Cytidylate kinase	5 µM	16	1163 ± 58	0.87 ± 0.01			
NagD	54.1	Ribonucleotide monophosphatase	Discarded due to non-uniform protein localization						
KdsB	54.6	3-deoxy-manno-octulosonate cytidylyltransferase	0 µM	11	1659 ± 70	0.84 ± 0.01			
Map	56.3	Methionine aminopeptidase	0 µM	20	1830 ± 78	0.81 ± 0.01			
MmuM	60.4	Homocysteine S-methyltransferase	5 µM	14	2241 ± 138	0.73 ± 0.01			
RihA	60.8	Pyrimidine-specific ribonucleoside hydrolase	Discarded due to non-uniform protein localization						
PanE	60.8	2-dehydropantoate 2-reductase	0 µM (5 µM)	18	1059 ± 26	0.85 ± 0.01	7.8 ± 0.2	11	5.2 ± 0.6
SolA	67.9	N-methyl-L-tryptophan oxidase	0 µM	7	795 ± 31	0.82 ± 0.01	9.9 ± 0.5		
Pgk	68.1	Phosphoglycerate kinase	0 µM	16	991 ± 41	0.90 ± 0.01	8.6 ± .0.3		
EntC	69.9	Isochorismate synthase	15 µM	15	1777 ± 119	0.82 ± 0.01			
AroA	73.1	3-phosphoshikimate 1-carboxyvinyltransferase	0 µM	9	995 ± 69	0.86 ± 0.01	8.7 ± 0.7		
ThrC	74.1	Threonine synthase	0 µM	14	908 ± 28	0.87 ± 0.01	9.1 ± 0.3		
MurF	74.4	UDP-N-acetylmuramoyl-tripeptide--D-alanyl-D-alanine ligase	0 µM	7	1008 ± 76	0.85 ± 0.02	8.3 ± 0.7		
DsdA	74.9	D-serine dehydratase	0 µM	14	1017 ± 53	0.89 ± 0.01	8.4 ± 0.4	10	7.8 ± 0.7
HemN	79.7	Oxygen-independent coproporphyrinogen III oxidase	0 µM	13	1262 ± 54	0.86 ± 0.01	6.7 ± 0.4		
PrpD	80.9	2-methylcitrate dehydratase	0 µM	12	1866 ± 140	0.84 ± 0.01			
DnaK	96.0	Molecular chaperone	5 µM	10	2296 ± 78	0.76 ± 0.01			
MalZ	96.0	Maltodextrin glucosidase	0 µM	9	3725 ± 229	0.77 ± 0.01			
GlcB	107.5	Malate synthase G	5 µM (15 µM)	16	1315 ± 45	0.86 ± 0.01	6.4 ± 0.2	10	6.7 ± 1.1
MetE	111.7	5-methyltetrahydropteroyltriglutamate--homocysteine methyltransferase	0 µM	8	1137 ± 53	0.87 ± 0.01	7.4 ± 0.3		
LeuS	124.2	Leucine--tRNA ligase	0 µM	14	1637 ± 75	0.86 ± 0.01	5.1 ± 0.2		
AcnA	124.7	Aconitate hydratase A	5 µM (15 µM)	19	1415 ± 56	0.86 ± 0.01	6.1 ± 0.2	10	4.3 ± 0.4
MetH	163.0	Methionine synthase	0 µM (5 µM)	9	1402 ± 45	0.81± 0.01	5.8 ± 0.1	15	4.0 ± 0.5

986 **Figure 1 – supplementary table 2. Strains and plasmids used in this study**

Strain or plasmid	Relevant genotype or phenotype	Reference or source
	Strains	
E. coli W3110	W3110 derivative with functional RpoS [rpoS396(Am)]	(Serra Diego et al.)
NB63	W3110 Δ*clpA*	This work
	Plasmids	
pTrc99A	Amp^r; expression vector; pBR ori; *trc* promoter, IPTG inducible	(Amann, Ochs, and Abel 1988)
pCP20	Amp^r, Cam^r; *flp*	(Cherepanov and Wackernagel 1995)
pNB1	Amp^r; *sfGFP* in pTrc99A	This work
pNB3	Amp^r; *Adk-sfGFP* in pTrc99A	This work
pNB4	Amp^r; *CoaE-sfGFP* in pTrc99A	This work
pNB5	Amp^r; *Cmk-sfGFP* in pTrc99A	This work
pNB6	Amp^r; *Pgk-sfGFP* in pTrc99A	This work
pNB7	Amp^r; *MmuM-sfGFP* in pTrc99A	This work
pNB8	Amp^r; *PrpD-sfGFP* in pTrc99A	This work
pNB9	Amp^r; *DsdA-sfGFP* in pTrc99A	This work
pNB11	Amp^r; *GlcB-sfGFP* in pTrc99A	This work
pNB13	Amp^r; *HemN-sfGFP* in pTrc99A	This work
pNB14	Amp^r; *Map^{WT}-sfGFP* in pTrc99A	This work
pNB15	Amp^r; *ThrC-sfGFP* in pTrc99A	This work
pNB16	Amp^r; *MalZ-sfGFP* in pTrc99A	This work
pNB17	Amp^r; *EntC-sfGFP* in pTrc99A	This work
pNB18	Amp^r; *ThpR-sfGFP* in pTrc99A	This work
pNB19	Amp^r; *AroA-sfGFP* in pTrc99A	This work
pNB20	Amp^r; *ClpS^{WT}-sfGFP* in pTrc99A	This work
pNB21	Amp^r; *Crr-sfGFP* in pTrc99A	This work
pNB22	Amp^r; *KdsB-sfGFP* in pTrc99A	This work
pNB23	Amp^r; *LeuS-sfGFP* in pTrc99A	This work
pNB24	Amp^r; *MurF-sfGFP* in pTrc99A	This work
pNB25	Amp^r; *NagD-sfGFP* in pTrc99A	This work
pNB26	Amp^r; *RihA-sfGFP* in pTrc99A	This work
pNB27	Amp^r; *SolA-sfGFP* in pTrc99A	This work
pNB28	Amp^r; *UbiC-sfGFP* in pTrc99A	This work
pNB29	Amp^r; *PanE-sfGFP* in pTrc99A	This work
pNB30	Amp^r; *FolK-sfGFP* in pTrc99A	This work
pNB39	Amp^r; *AcnA-sfGFP* in pTrc99A	This work
pNB40	Amp^r; *MetE-sfGFP* in pTrc99A	This work
pNB42	Amp^r; *MetH-sfGFP* in pTrc99A	This work
pNB44	Amp^r; *YggX-sfGFP* in pTrc99A	This work
pNB45	Amp^r; *Adk$^{C.c.}$-sfGFP* in pTrc99A	This work
pNB46	Amp^r; *Adk$^{V.c.}$-sfGFP* in pTrc99A	This work
pNB47	Amp^r; *Adk$^{M.x.}$-sfGFP* in pTrc99A	This work
pNB48	Amp^r; *AcnA$^{M.x.}$-sfGFP* in pTrc99A	This work
pNB49	Amp^r; *AcnA$^{V.c.}$-sfGFP* in pTrc99A	This work
pNB51	Amp^r; *Adk$^{B.s.}$-sfGFP* in pTrc99A	This work
pNB52	Amp^r; *AcnA$^{B.s.}$-sfGFP* in pTrc99A	This work
pNB54	Amp^r; *Adk$^{Y.e.}$-sfGFP* in pTrc99A	This work
pNB56	Amp^r; *Pgk$^{C.c.}$-sfGFP* in pTrc99A	This work
pNB58	Amp^r; *Pgk$^{V.c.}$-sfGFP* in pTrc99A	This work
pNB59	Amp^r; *Pgk$^{M.x.}$sfGFP* in pTrc99A	This work
pNB60	Amp^r; *AcnA$^{Y.e.}$-sfGFP* in pTrc99A	This work
pNB61	Amp^r; *DnaK^{WT}-sfGFP* in pTrc99A	This work
pNB62	Amp^r; *Map^{K211E_K218E_K224E_K226E}-sfGFP* in pTrc99A	This work
pNB63	Amp^r; *Map^{K211A_K218A_K224A_K226A}-sfGFP* in pTrc99A	This work
pNB64	Amp^r; *DnaK^{V436F} -sfGFP* in pTrc99A	This work
pNB66	Amp^r; *ClpS^{D35A_D36A_H66A}-sfGFP* in pTrc99A	This work

987

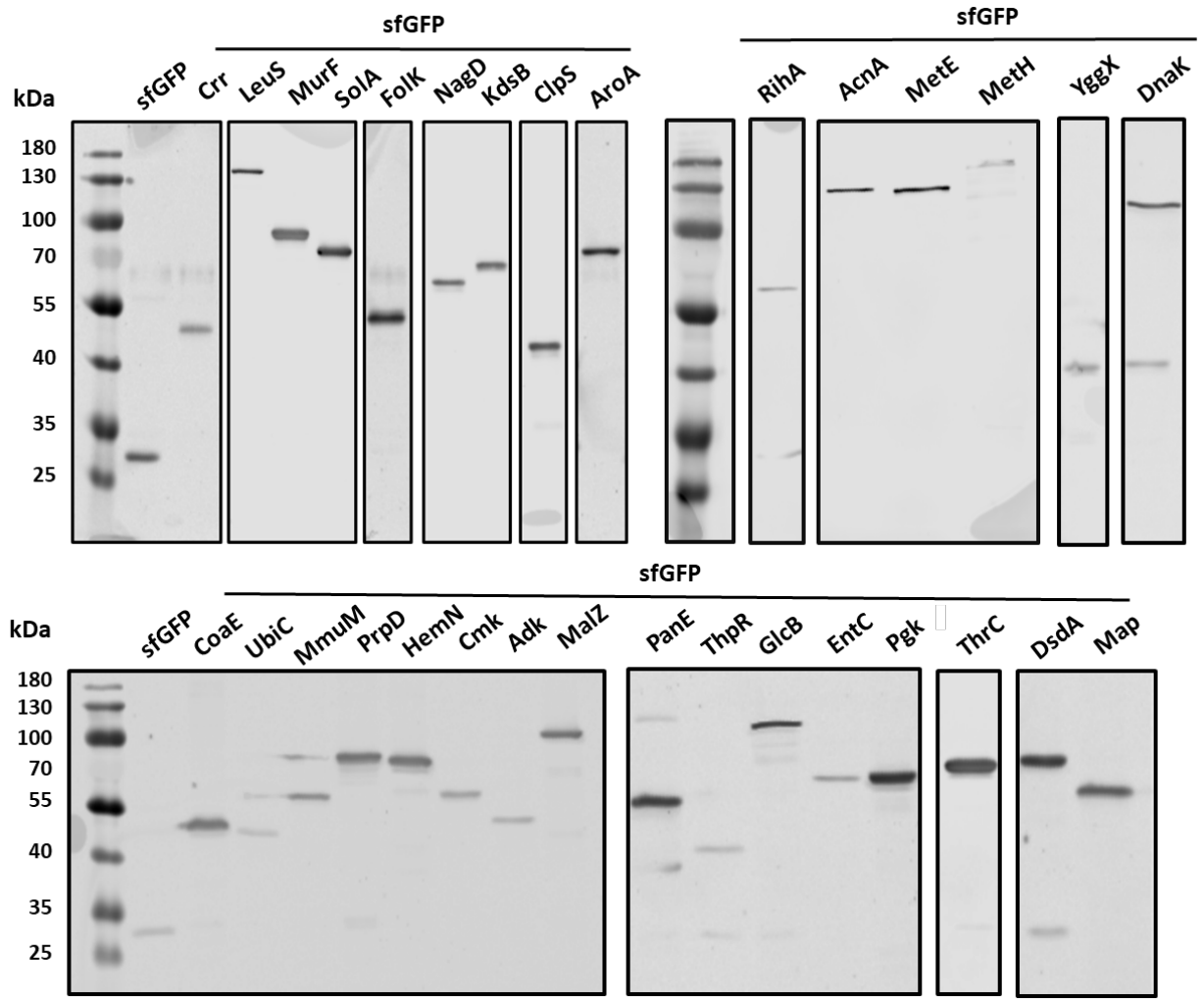

Figure 1 – figure supplement 1. Expression analysis for all *E. coli* protein constructs made in this study. Expression of proteins was analyzed by SDS-PAGE and immunoblotting using a primary antibody specific for GFP. All fusion proteins displayed a dominant band corresponding to the expected molecular mass of the full-length fusion (Figure 1 – supplementary table 1).

Figure 1 – figure supplement 1 – source data 1-10. Raw images of immunoblots used for Figure 1 – figure supplement 1.

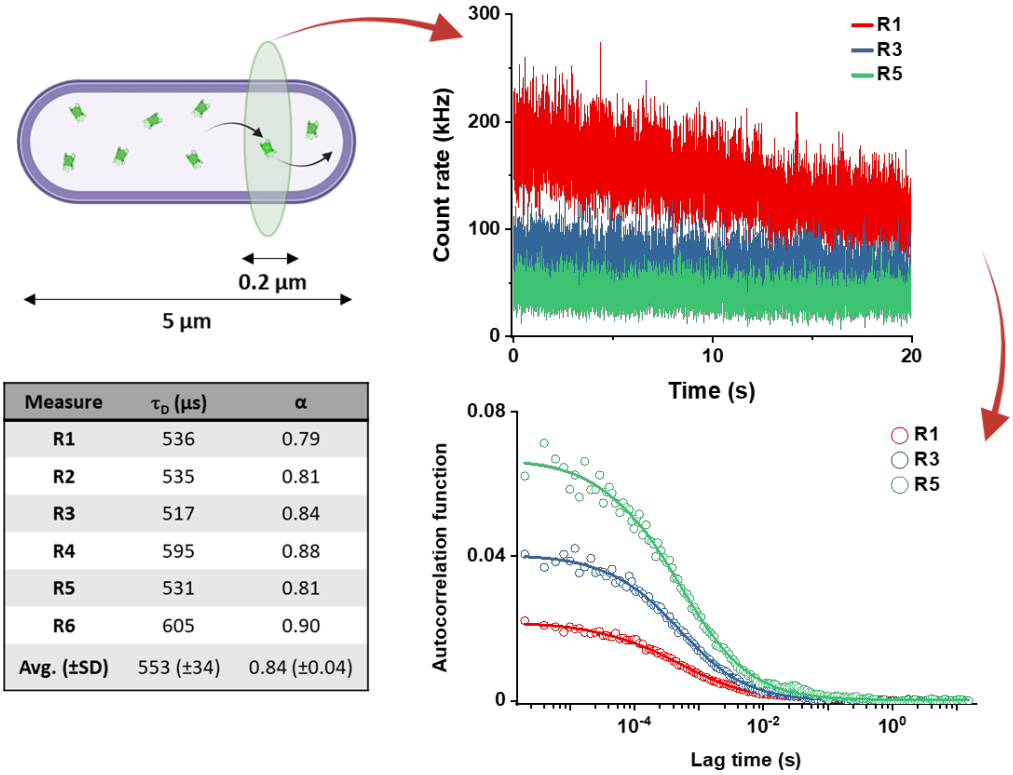

Measure	τ_D (µs)	α
R1	536	0.79
R2	535	0.81
R3	517	0.84
R4	595	0.88
R5	531	0.81
R6	605	0.90
Avg. (±SD)	553 (±34)	0.84 (±0.04)

Figure 1 – figure supplement 2. Workflow of a typical FCS experiment. The focus of the confocal microscope is positioned near one pole in the cell of interest, and six subsequent acquisitions of the fluorescence intensity of 20 seconds each are performed. The example for sfGFP shows only traces for R1, R3 and R5 measurements (different colors). The autocorrelation functions (ACFs) are then calculated independently for each acquisition. The values for τ_D and α are extracted independently from the fit to each ACF using the anomalous diffusion model (solid lines) and then averaged to obtain the τ_D and α for each individual cell.

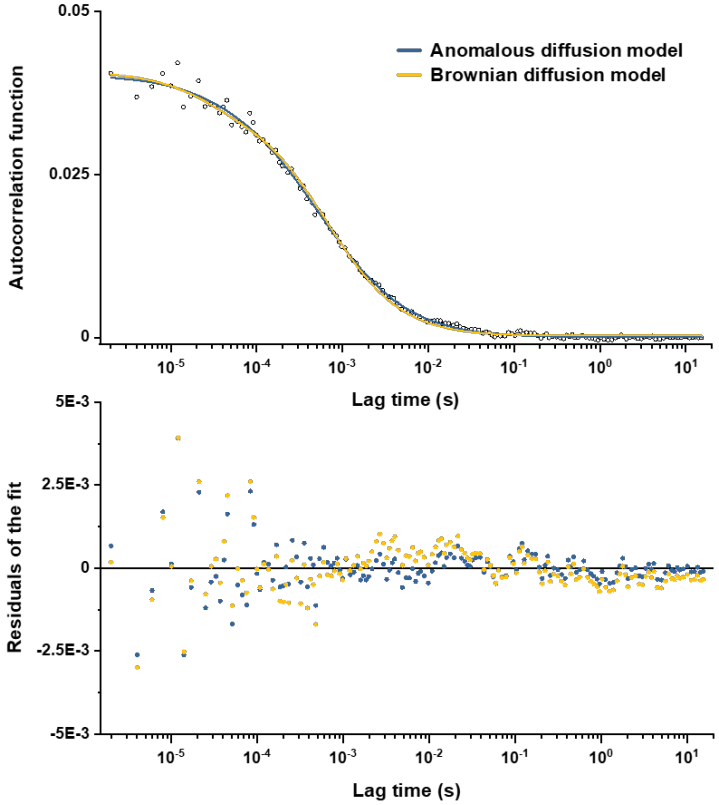

Figure 1 – figure supplement 3. Comparison between fits of the experimental data with Brownian and anomalous diffusion models. The experimental data (here the example for the R3 measurement from Figure 1 – figure supplement 2) were fitted by the model of free Brownian diffusion and by the anomalous diffusion model as indicated by different colors (upper panel), with the corresponding values of residuals (lower panel).

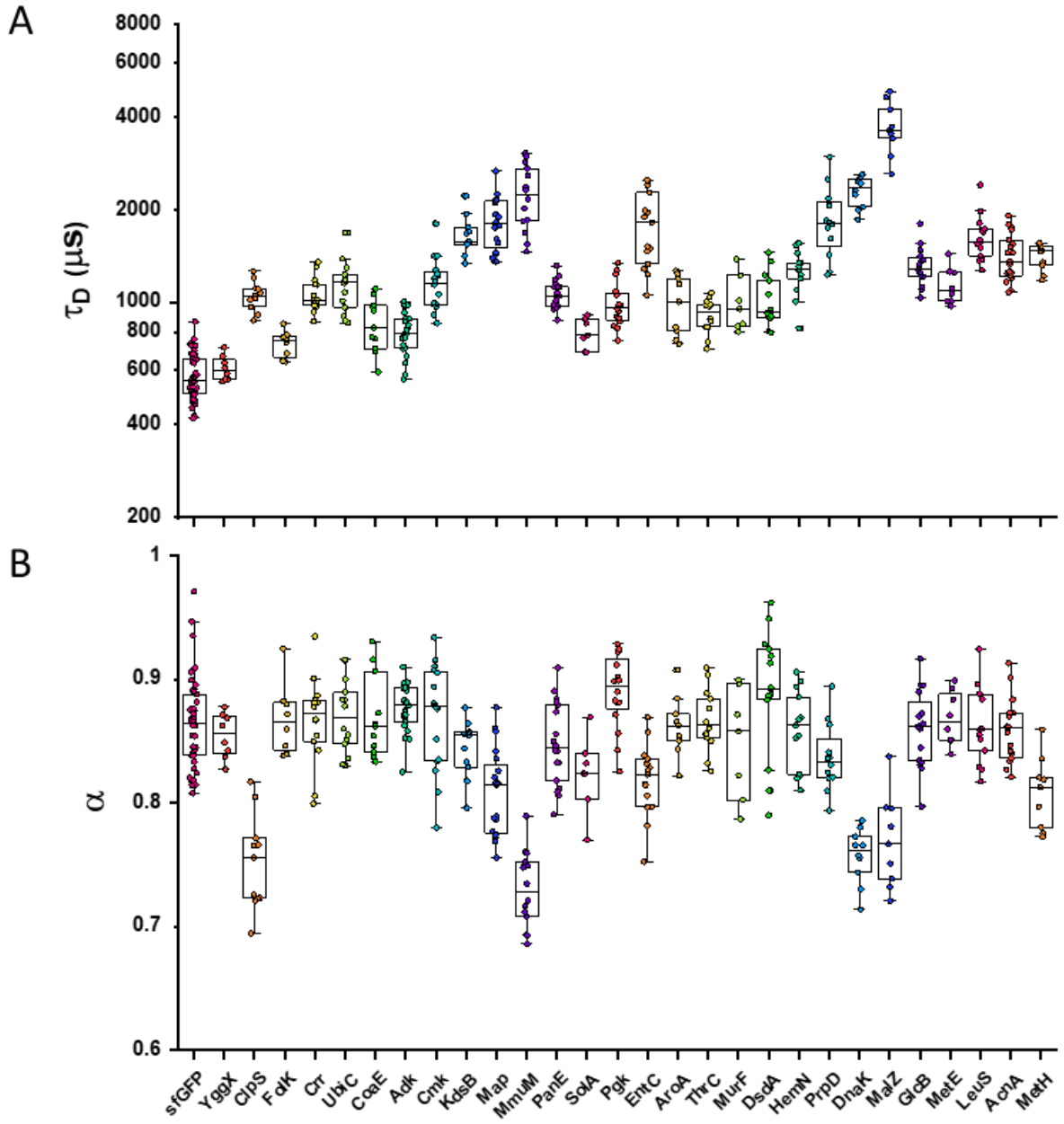

1007

1008 **Figure 1 – figure supplement 4. Individual measurements of τ_D and α for all *E. coli* protein constructs included**

1009 **in the analysis of mass dependence.** Each dot in the box plot represents the values of τ_D (A) and α (B) for one

1010 individual cell. The averages values calculated from these datasets are shown in Figure 1.

1011 **Figure 1 – figure supplement 4 – source data 1.** Original values used for plots in Figure 1 – figure supplement 4.

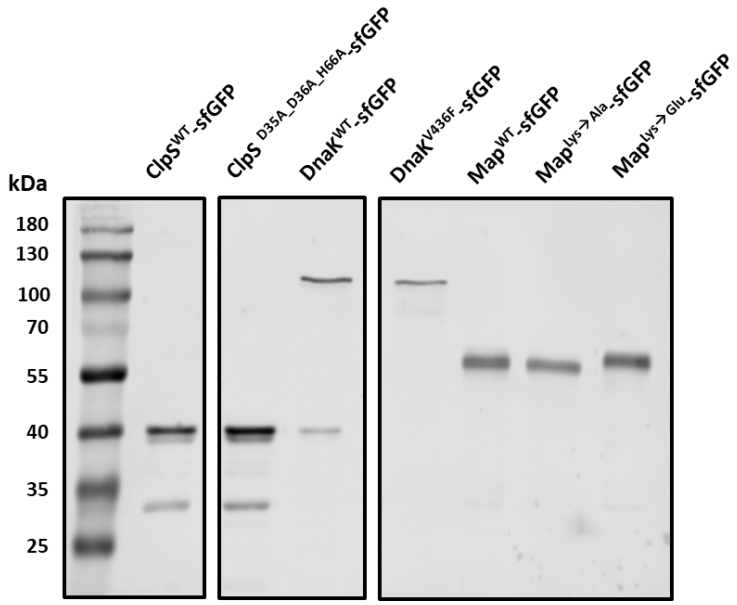

Figure 1 – figure supplement 5. Expression analysis for the mutants with impaired interactions. The expression of indicated point mutants of ClpS, DnaK and Map was analyzed by SDS-PAGE and immunoblotting using a primary antibody specific for GFP. All mutants displayed a dominant band corresponding to the expected molecular mass of the full-length fusion, and comparable to that of the wild-type counterpart. ClpS^{D35A_D36A_H66A}-sfGFP was measured in the same *ΔclpA* background as subsequently used for the FCS experiments.

Figure 1 – figure supplement 5 – source data 1-2. Raw images of immunoblots used for Figure 1 – figure supplement 5.

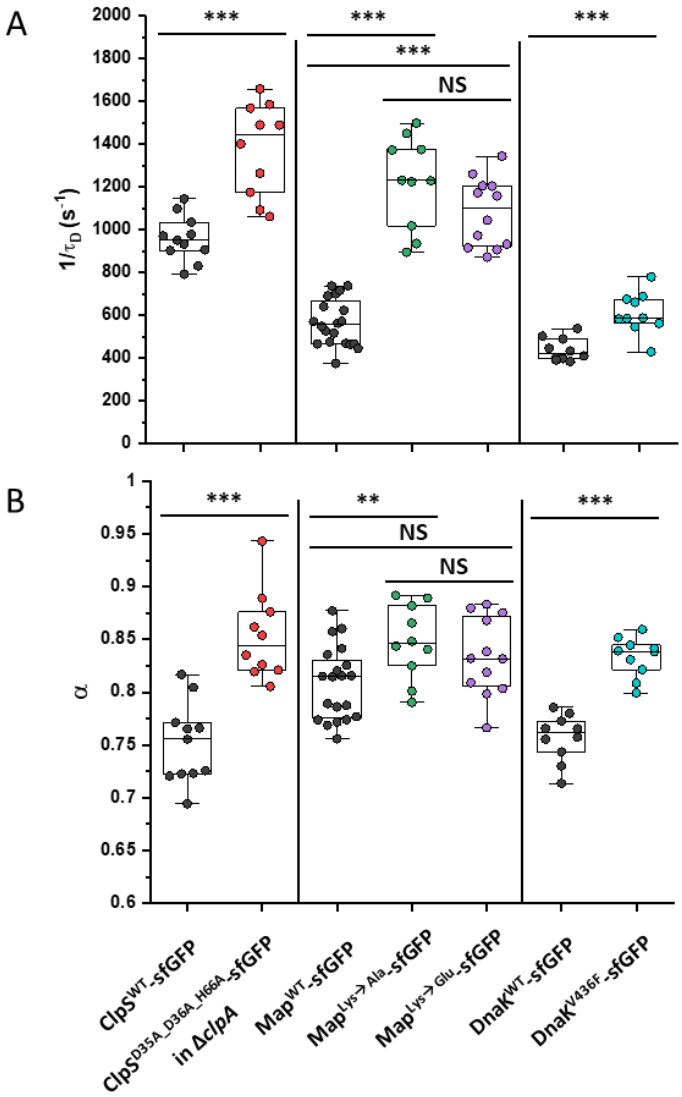

1020

1021 **Figure 1 – figure supplement 6. Mobility of ClpS, Map and DnaK and of indicated mutants with disrupted**

1022 **protein interactions.** Each dot in the box plot represents the values of τ_D (A) and α (B) for one individual cell. ClpS

1023 mutant was measured in *ΔclpA* background. *** p<0.0001; * p<0.05; NS: no statistically significant difference in a

1024 two-tailed heteroscedastistic *t*-test.

1025 **Figure 1 – figure supplement 6 – source data 1.** Original values used for plots in Figure 1 – figure supplement 6.

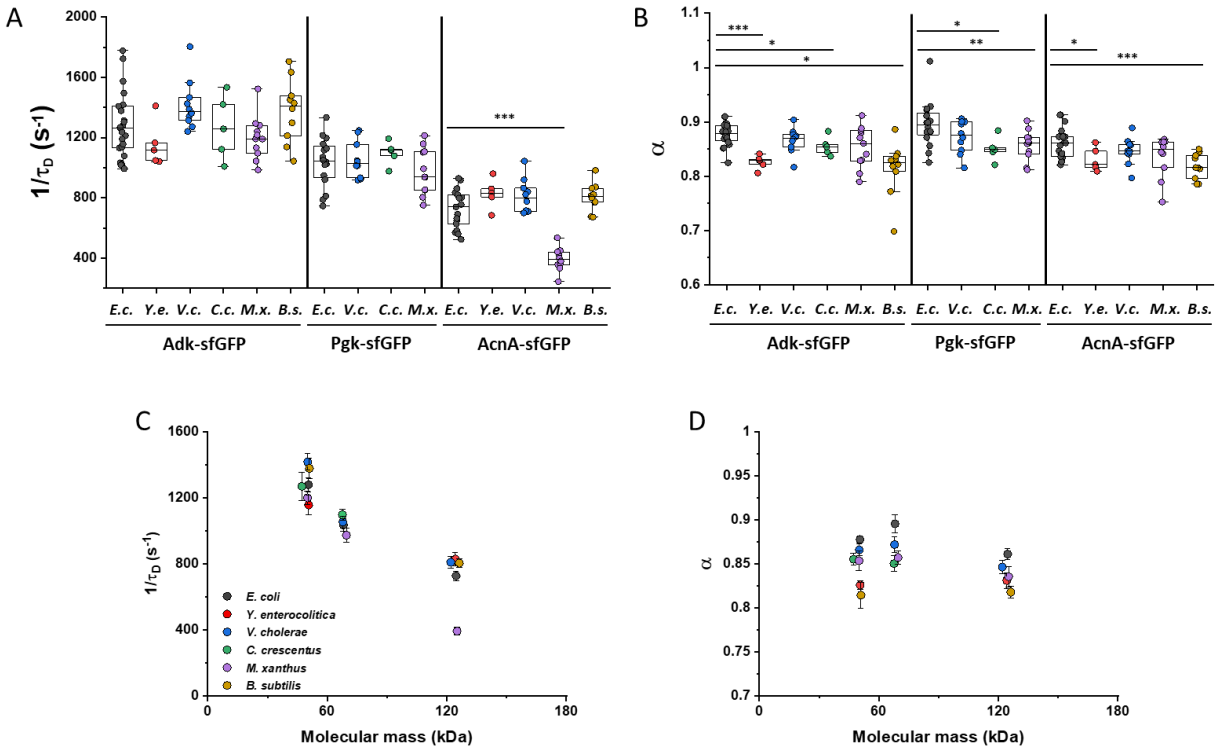

1026

1027 **Figure 1 – figure supplement 7. Mobility of homologous proteins from other bacterial species in *E. coli*.** The
1028 mobility (A) and anomalous diffusion exponent (B) of sfGFP fusions to homologues of Adk, Pgk and AcnA from
1029 indicated bacterial species (*E.c. = Escherichia coli; Y.e. = Yersinia enterocolitica; V.c. = Vibrio cholerae; C.c. =*
1030 *Caulobacter crescentus; M.x. = Myxococcus xanthus; B.s. = Bacillus subtilis*) compared with that of their counterpart
1031 from *E. coli*. *** $p<0.0001$; ** $p<0.001$; * $p<0.05$ in a two-tailed heteroscedastistic *t*-test. When not indicated, no
1032 statistically significant difference is observed. (C, D) Mass dependence of diffusion parameters of these sfGFP-
1033 constructs. Each symbol represents the average value for all individual cells that have been measured for that construct
1034 and the error bars represent the standard error of the mean.

1035 **Figure 1 – figure supplement 7 – source data 1.** Original values used for plots in Figure 1 – figure supplement 7.

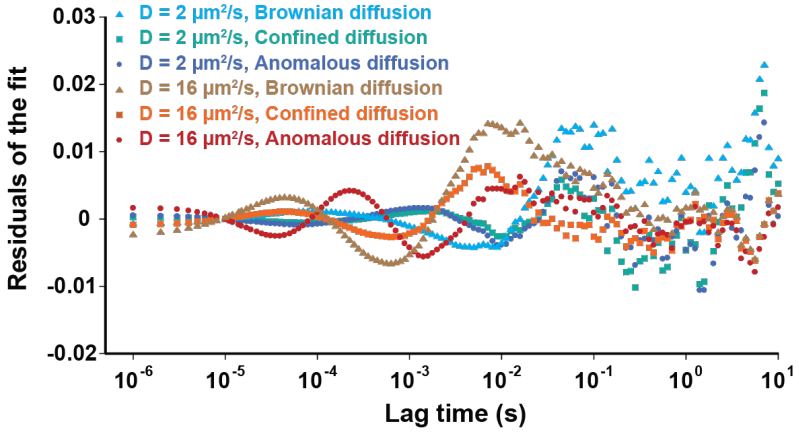

Figure 2 – figure supplement 1. Residuals of fitting the simulated ACFs with different models. Simulated fluorescence intensity ACF data were fitted by the models of anomalous and Brownian diffusion, as well as by the OU model of Brownian diffusion under confinement, as indicated.

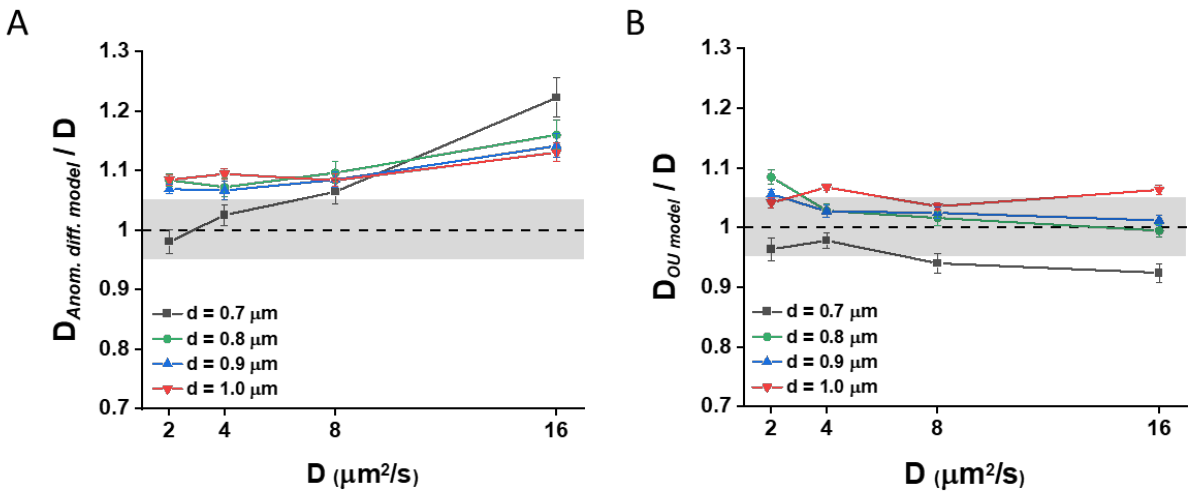

1040

1041 **Figure 2 – figure supplement 2. Diffusion coefficients fitted from simulation data.** Diffusion coefficients
1042 computed ($D = \omega_0^2/4\tau_D$) from the diffusion times extracted from the fit of the Brownian simulation data with (A) the
1043 anomalous diffusion model or (B) the Ornstein-Uhlenbeck (OU) model of Brownian diffusion under confinement at
1044 various value of the ansatz *D* and of the cell diameter d, normalized by the ansatz *D*. The grey areas represent ± 5%
1045 accuracy.

1046 **Figure 2 – figure supplement 2 – source data 1.** Original values used for plots in Figure 2 – figure supplement 2.

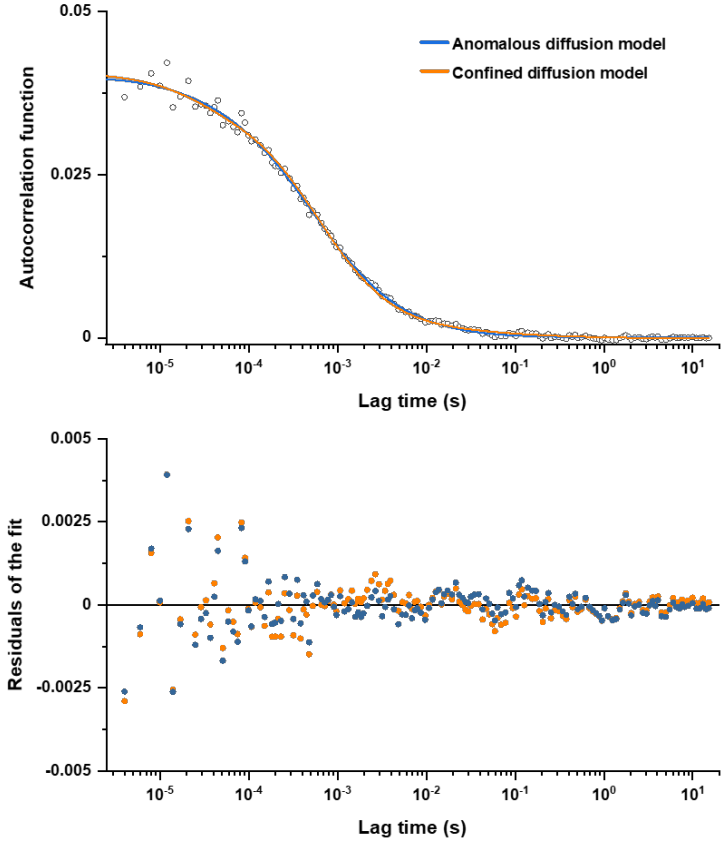

1047

1048 **Figure 2 – figure supplement 3. Comparison between fits of the experimental data with confined diffusion and**
1049 **anomalous diffusion models.** The experimental data (here the example for the R3 measurement from Figure 1 –
1050 figure supplement 2) were fitted by the model of confined diffusion and by the anomalous diffusion model as indicated
1051 by different colors (upper panel), yielding comparable values of residuals (lower panel).

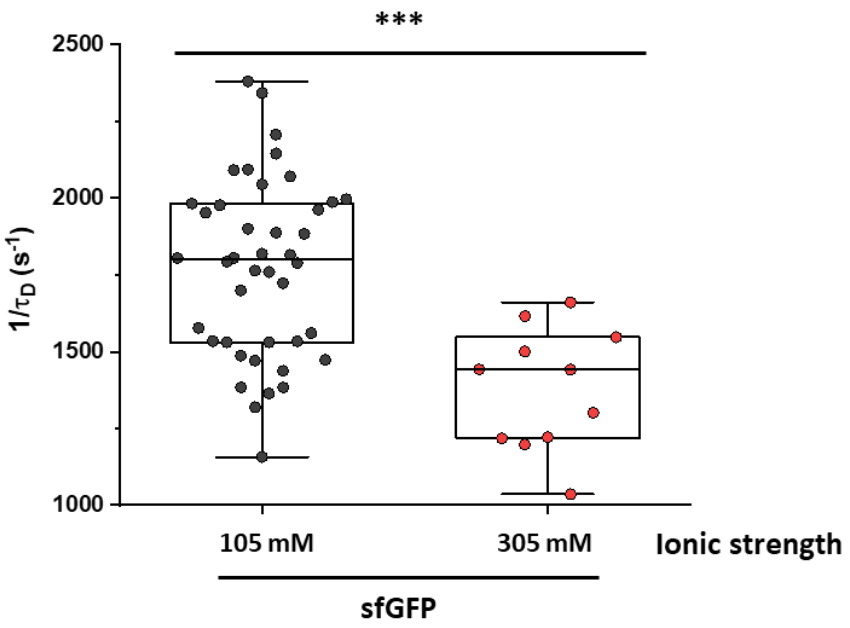

1052

1053 **Figure 4 – figure supplement 1. Effect of osmotic upshift on protein mobility.** The effect of osmotic upshift on
1054 sfGFP mobility, measured in cells that were either resuspended in tethering buffer (ionic strength of 105 mM) or in
1055 the same buffer but supplemented with additional 100 mM NaCl (total ionic strength of 305 mM). *** $p<0.0001$ in a
1056 two-tailed heteroscedastistic *t*-test.

1057 **Figure 4 – figure supplement 1 – source data 1.** Original values used for plots in Figure 4 – figure supplement 1.

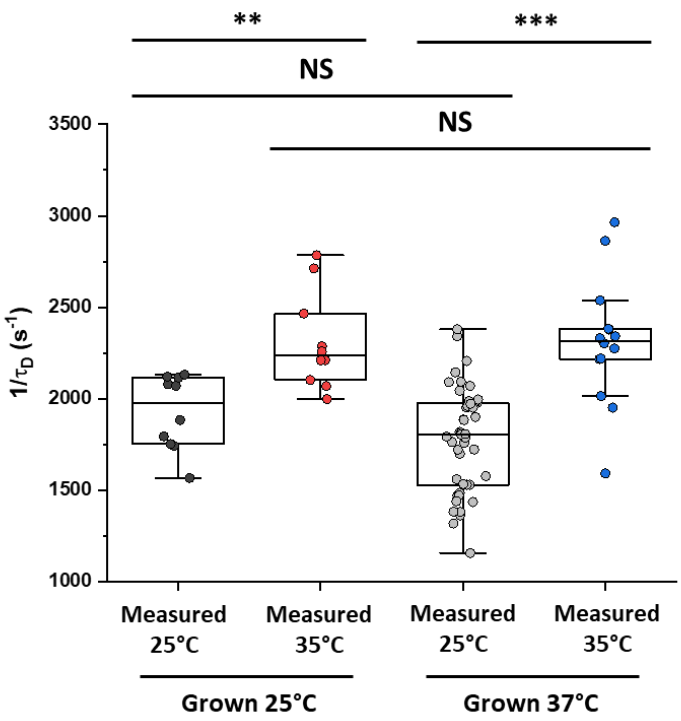

1058

1059 **Figure 4 – figure supplement 2. Effect of growth and measurement temperature on protein diffusion.** Mobility

1060 for sfGFP in cells grown either at 25°C or at 37°C and measured either at 25°C or at 35°C, as in Figure 4A. ***

1061 p<0.0001; ** p<0.001; NS: no statistically significant difference in a two-tailed heteroscedastistic *t*-test.

1062 **Figure 4 – figure supplement 2 – source data 1.** Original values used for plots in Figure 4 – figure supplement 2.

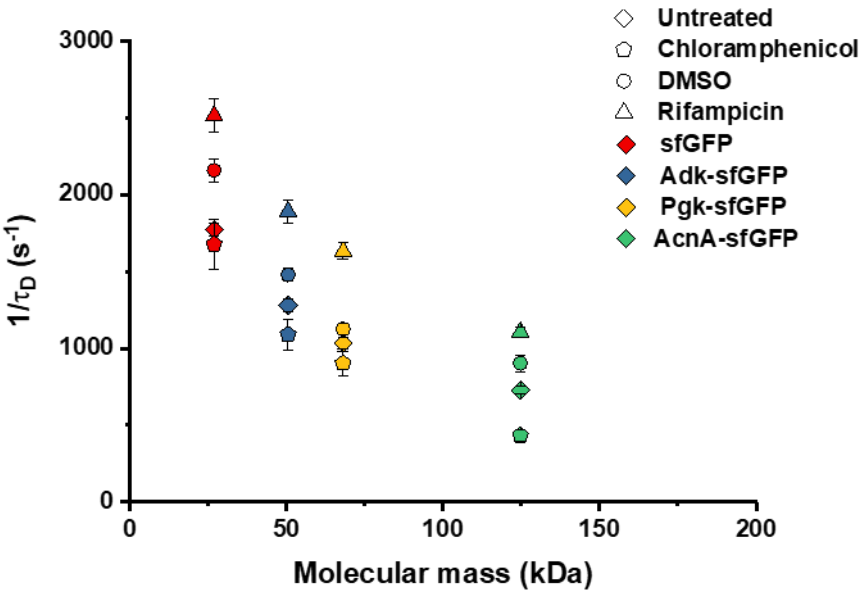

1063

1064 **Figure 4 – figure supplement 3. Mass dependence of the effect of antibiotics on protein diffusion.** Data from

1065 Figure 4B were plotted as a function of molecular mass for indicated protein constructs and treatments. Error bars

1066 represent the standard error of the mean.

1067 **Figure 4 – figure supplement 3 – source data 1.** Original values used for plots in Figure 4 – figure supplement 3.

Appendix 1

Notes on the acquisition and analysis protocols for FCS measurements in bacterial cells

Due to the limited size of bacterial cells, FCS measurements require precise positioning of the confocal volume in the bacterial cytoplasm and minimization of the photobleaching-induced effects. In order to ensure that, before fitting an autocorrelation function, we verified the stability of the lateral (*xy*) positioning of the observation volume by visually analyzing for lateral drifts in confocal images acquired immediately before and after the FCS acquisition. This was done by annotating the *xy* position in the pre-aquisition image and verifying that the positioning did not change in the post-aquisition image after 120 seconds. Measurements showing *xy* drift were excluded from the analysis (Appendix 1 - figure 1). Furthermore, the focal stability of the sample was increased by thermal equilibration on the microscope stage before measurements.

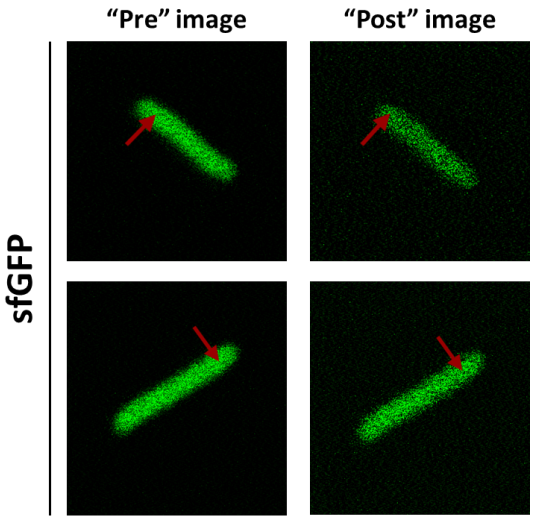

Appendix 1 - figure 1. Typical examples of presence or absence of lateral focal drift during FCS measurements. Substantial lateral drift could be observed for <10% of experiments (upper images), whereas most measurement showed no perceptible lateral drift (lower images).

17 Long-term photobleaching due to the progressive decrease of the total number of fluorescent
18 proteins during FCS experiments (Appendix 1 - figure 2) is unavoidable due to the small volume
19 of *E. coli* cells, and it requires correction to avoid artifacts. We observed that almost identical ACFs
20 were obtained when correcting for the photobleaching using either multi-segment detrending (Jay
21 Unruh, https://research.stowers.org/imagejplugins/index.html, Stowers Institute for Medical
22 Research, USA) or a local averaging approach (Wachsmuth et al. 2015) (Appendix 1 - figure 3).

23

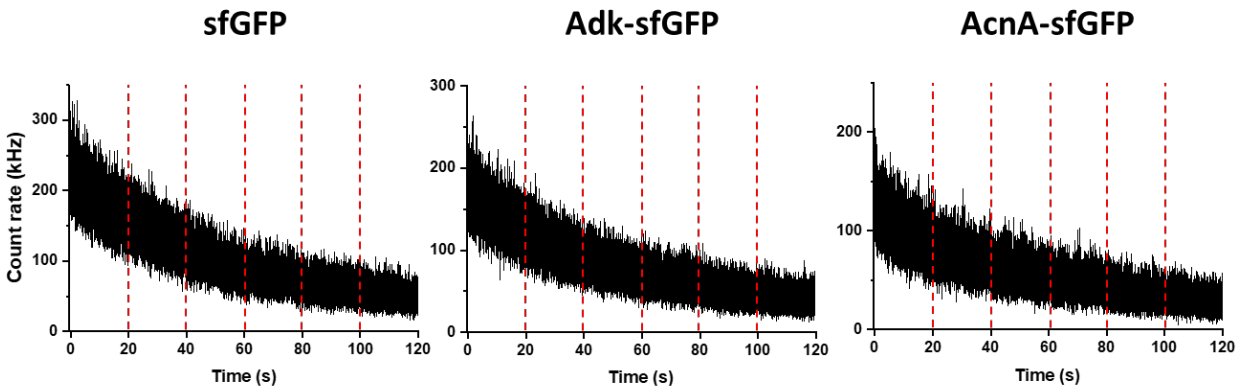

24

25 **Appendix 1 - figure 2. Typical traces of fluorescence intensity during FCS measurements.** Examples of
26 fluorescence intensity traces for indicated protein fusions. The vertical red dashed lines separate sequential
27 fluorescence intensity acquisitions on the same cell.

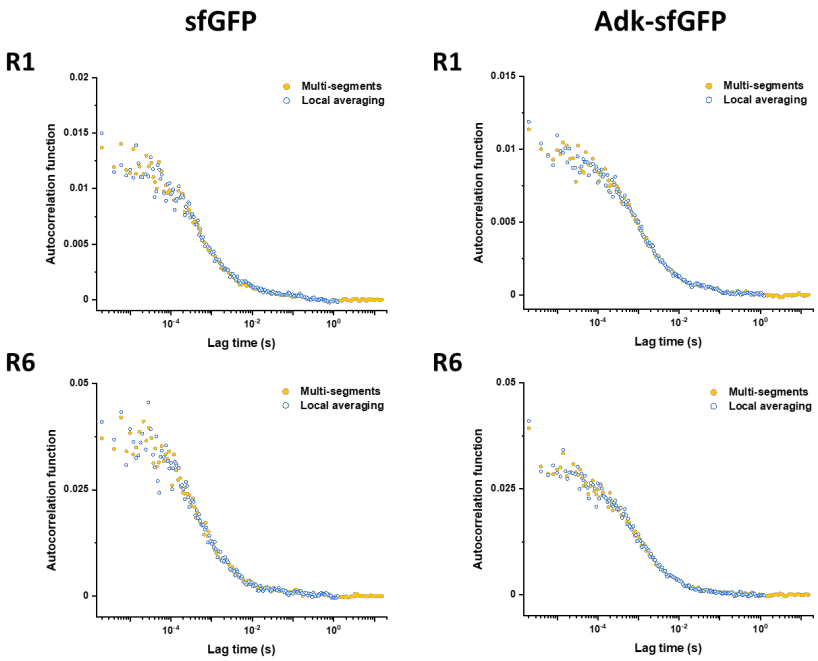

Appendix 1 - figure 3. Results of detrending with multi-segments and local averaging approaches. Comparison of experimental ACFs corrected using either multi-segments or local averaging approaches (as indicated) for sfGFP and Adk-sfGFP and different data acquisition segments (R1 vs R6).

We also confirmed that there was no systematic trend in the fitted values of τ_D and α with the time of the fluorescence trace acquisition (Appendix 1 - figure 4). An additional process that could potentially affect autocorrelation functions is short-term photobleaching of the fluorophore in the confocal volume, also known as cryptic photobleaching, which can artificially accelerate the decrease of the autocorrelation function and lead to an underestimation of the protein residence time (Macháň, Foo, and Wohland 2016). This process is different from long-term photobleaching, which is caused by the continuous illumination in the entire illumination light cone. However, the effect of cryptic photobleaching was shown to be typically <5%, even for proteins that diffuse 10 to 100 times slower and have higher bleaching rates than our constructs (Stasevich et al. 2010; Wachsmuth et al. 2015).

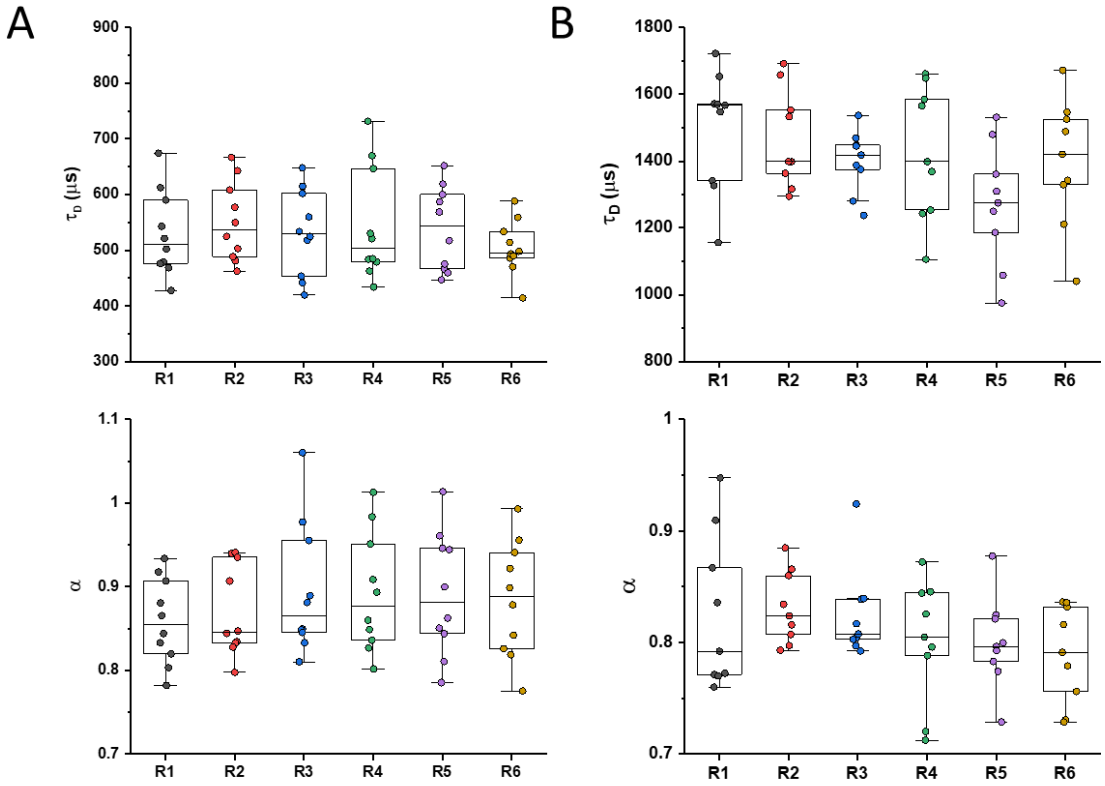

Appendix 1 - figure 4. Values of τ_D or α for the six sequential ACFs. Values were determined by fitting the anomalous diffusion model to experimental ACFs for the six sequential time segments per individual cell expressing sfGFP (A) or MetH-sfGFP (B).

Appendix 2

Ornstein-Uhlenbeck model for confinement effect in FCS measurements

We aim to derive the autocorrelation function for an FCS experiment in which the fluorescent particles are confined by a (possibly anisotropic) harmonic potential centered at $(x, y, z) = (0,0,0)$, i.e.

$$V(x, y, z) = \frac{k_x x^2}{2} + \frac{k_y y^2}{2} + \frac{k_z z^2}{2}$$

where k_i represents the stiffness of the potential in each dimension, and thus the extent σ_i of confinement along that dimension given by $\sigma_i^2 \equiv k_\mathrm{B}T/k_i$.

We can treat each dimension independently, using x without loss of generality in what follows. Diffusion in a harmonic potential is described by the Ornstein-Uhlenbeck process. The corresponding Green's function $P(x, t|x_0)$, representing the probability of finding a particle at position x at time t given that it was at position x_0 at time $t = 0$, is

$$P(x, t|x_0) = \frac{1}{\sqrt{2\pi\sigma_x^2\left(1 - e^{-\frac{2Dt}{\sigma_x^2}}\right)}} \exp\left[-\frac{1}{2\sigma_x^2}\frac{\left(x - x_0 e^{-\frac{Dt}{\sigma_x^2}}\right)^2}{1 - e^{-\frac{2Dt}{\sigma_x^2}}}\right]$$

at long times, $t \to \infty$, we recover the stationary state given by the Boltzmann distribution corresponding to the harmonic trap

$$P_\mathrm{st}(x) = \frac{1}{\sqrt{2\pi\sigma_x^2}} \exp\left[-\frac{x^2}{2\sigma_x^2}\right].$$

The autocorrelation function (ACF) $G(t)$ of an FCS measurement is given as the multiple integral over the product of the probability to detect a photon from a molecule at some initial position x_0, the probability density that it diffuses from this position to a final position x within time t (given by Green's function), and the probability to detect a photon from a molecule at this final position (Enderlein et al. 2005; Enderlein 2012). Note that the probability of detection of a molecule will necessarily be proportional to the intensity of the laser beam, which we can assume Gaussian and also centered at $(x, y, z) = (0,0,0)$, with the usual form

$$I(x, y, z) = I_0 \exp\left(-\frac{2x^2}{\omega_0^2}\right) \exp\left(-\frac{2y^2}{\omega_0^2}\right) \exp\left(-\frac{2z^2}{S^2\omega_0^2}\right) \equiv I_0 I_x(x) I_y(y) I_z(z)$$

where ω_0 is the width of the (circular) laser beam along the x and y directions, and S is a dimensionless factor accounting for the anisotropy along the z direction, i.e. the axial direction of the beam.

Ignoring constant normalization factors and baselines, the time dependent part of the autocorrelation function is then given by $G(t) = G_x(t) G_y(t) G_z(t)$ with

$$G_x(t) = \int \mathrm{d}x \int \mathrm{d}x_0 I_x(x) P(x, t|x_0) I_x(x_0) P_{\mathrm{st}}(x_0)$$

which can be directly integrated to give, after normalizing so that $G_x(t = 0) = 1$, the expression

$$G_x(t) = \left[1 + 2\frac{\sigma_x^2}{\omega_0^2} \frac{1 - e^{-\frac{2Dt}{\sigma_x^2}}}{1 + \frac{1}{8}\frac{\omega_0^2}{\sigma_x^2}}\right]^{-\frac{1}{2}}. \quad \text{(A2-1)}$$

Note that, in the limit of no confinement, $\sigma_x^2 \to \infty$, this equation reduces to the well-known ACF for unconfined diffusion

$$G_x(t) = \left[1 + \frac{4Dt}{\omega_0^2}\right]^{-\frac{1}{2}} = \left[1 + \frac{t}{\tau_D}\right]^{-\frac{1}{2}}$$

where we have defined the diffusion time $\tau_D \equiv \omega_0^2/(4D)$. With this definition, the ACF in Eq. (A2-1) can be rewritten as

$$G_x(t) = \left[1 + 2\frac{\sigma_x^2}{\omega_0^2}\frac{1 - e^{-\frac{1\omega_0^2}{2\sigma_x^2}\frac{t}{\tau_D}}}{1 + \frac{1}{8}\frac{\omega_0^2}{\sigma_x^2}}\right]^{-\frac{1}{2}}.$$

The full three-dimensional ACF is then, in general,

$$G(t) = \left[1 + 2\frac{\sigma_x^2}{\omega_0^2}\frac{1 - e^{-\frac{1\omega_0^2}{2\sigma_x^2}\frac{t}{\tau_D}}}{1 + \frac{1}{8}\frac{\omega_0^2}{\sigma_x^2}}\right]^{-\frac{1}{2}}\left[1 + 2\frac{\sigma_y^2}{\omega_0^2}\frac{1 - e^{-\frac{1\omega_0^2}{2\sigma_y^2}\frac{t}{\tau_D}}}{1 + \frac{1}{8}\frac{\omega_0^2}{\sigma_y^2}}\right]^{-\frac{1}{2}}\left[1 + 2\frac{\sigma_z^2}{S^2\omega_0^2}\frac{1 - e^{-\frac{1\omega_0^2}{2\sigma_z^2}\frac{t}{\tau_D}}}{1 + \frac{1}{8}\frac{S^2\omega_0^2}{\sigma_z^2}}\right]^{-\frac{1}{2}}.$$

The cylindrical geometry of a bacterium can be approximated by an infinite cylinder along the y direction, so that $\sigma_x = \sigma_z = \sigma$ and $\sigma_y \to \infty$, resulting in the ACF

$$G(t) = \left[1 + 2\frac{\sigma^2}{\omega_0^2}\frac{1-e^{-\frac{1\omega_0^2}{2\sigma^2}\frac{t}{\tau_D}}}{1+\frac{1\omega_0^2}{8\sigma^2}}\right]^{-\frac{1}{2}}\left[1 + \frac{t}{\tau_D}\right]^{-\frac{1}{2}}\left[1 + 2\frac{\sigma^2}{S^2\omega_0^2}\frac{1-e^{-\frac{1\omega_0^2}{2\sigma^2}\frac{t}{\tau_D}}}{1+\frac{1}{8}\frac{S^2\omega_0^2}{\sigma^2}}\right]^{-\frac{1}{2}}. \quad \text{(A2-2)}$$

Eq. (A2-2), with the added baseline and multiplicative correction accounting for particles in the non-fluorescent state, corresponds to Eq. (3) in the main text.

Appendix 3

Effective diffusion coefficient of two linked proteins

In previous work, we studied the diffusion of two spherical objects with radii a_1 and a_2, joined together by a flexible linker (Agudo-Canalejo and Golestanian 2020). In the limit of a rigid linker of length ℓ, the effective diffusion coefficient of the composite object goes as:

$$D \simeq \frac{k_{\mathrm{B}}T}{6\pi\eta a_1}\frac{a_1}{(a_1+a_2)}\left[1+2\frac{a_1a_2}{(a_1+a_2)(a_1+a_2+\ell)}-\frac{9}{8}\frac{a_1a_2(a_1-a_2)^2}{(a_1+a_2)^2(a_1+a_2+\ell)^2}\right] \quad \text{(A3-1)}$$

plus higher order correction terms of order $O\left(\frac{a_i^3}{(a_1+a_2+\ell)^3}\right)$.

We can then consider what is the effective diffusion coefficient of two proteins that are linked to each other. For that, we first need to connect the molecular mass to the effective radius of the protein. If we identify subunit 1 with GFP, and subunit 2 with the protein attached to it, and we call M_{GFP} the molecular mass of GFP and M_{tot} the total molecular mass (sum of GFP and the protein), we expect relations of the form

$$a_1 = CM_{\mathrm{GFP}}^{\beta}$$

$$a_2 = C(M_{\mathrm{tot}} - M_{\mathrm{GFP}})^{\beta}$$

where C is a proportionality constant assumed to be typical for all proteins (which is of order 1, with values reported in the literature of about 0.65 (Smilgies and Folta-Stogniew 2015), when the mass is in kDa and the radius is in nm), and β is the scaling exponent introduced in the main text. For the linker which is made of 6 amino-acids, we may use the typical conversion factor 0.35 nm/amino-acid to estimate $\ell \approx 2$ nm.

Plugging these expressions for a_1 and a_2 into Eq. (A3-1) above, one obtains an expression for the diffusion coefficient D as a function of M_{tot} that depends only on three parameters (since the molecular mass of GFP is known): (i) the diffusion coefficient of GFP $\frac{k_{\mathrm{B}}T}{6\pi\eta a_1}$, (ii) the exponent β, and (iii) the rescaled linker length ℓ/C.

Appendix 4

Exact p-values for all significance analyses

Figure 1C

Testing pair	*P-value*
sfGFP vs Adk-sfGFP	0.000000010
Adk-sfGFP vs AcnA-sfGFP	0.00000000044

Figure 1 – figure supplement 6A

Testing pair	*P-value*
$ClpS^{WT}$-sfGFP vs $ClpS^{D35A_D36A_H66A}$-sfGFP	0.000094
Map^{WT}-sfGFP vs $Map^{Lys\rightarrow Ala}$-sfGFP	0.0000012
Map^{WT}-sfGFP vs $Map^{Lys\rightarrow Glu}$-sfGFP	0.000000016
$Map^{Lys\rightarrow Ala}$-sfGFP vs $Map^{Lys\rightarrow Glu}$-sfGFP	0.10
$DnaK^{WT}$-sfGFP vs $DnaK^{V436F}$-sfGFP	0.00023

Figure 1 – figure supplement 6B

Testing pair	*P-value*
$ClpS^{WT}$-sfGFP vs $ClpS^{D35A_D36A_H66A}$-sfGFP	0.000014
Map^{WT}-sfGFP vs $Map^{Lys\rightarrow Ala}$-sfGFP	0.0092
Map^{WT}-sfGFP vs $Map^{Lys\rightarrow Glu}$-sfGFP	0.065
$Map^{Lys\rightarrow Ala}$-sfGFP vs $Map^{Lys\rightarrow Glu}$-sfGFP	0.37
$DnaK^{WT}$-sfGFP vs $DnaK^{V436F}$-sfGFP	0.00000019

Figure 1 – figure supplement 7A

Testing pair	*P-value*
$Adk^{E.c.}$-sfGFP vs $Adk^{Y.e.}$-sfGFP	0.17
$Adk^{E.c.}$-sfGFP vs $Adk^{V.c.}$ -sfGFP	0.056
$Adk^{E.c.}$-sfGFP vs $Adk^{C.c.}$-sfGFP	0.93
$Adk^{E.c.}$-sfGFP vs $Adk^{M.x.}$-sfGFP	0.21
$Adk^{E.c.}$-sfGFP vs $Adk^{B.s.}$-sfGFP	0.23
$Pgk^{E.c.}$-sfGFP vs $Pgk^{V.c.}$-sfGFP	0.75
$Pgk^{E.c.}$-sfGFP vs $Pgk^{C.c.}$-sfGFP	0.26
$Pgk^{E.c.}$-sfGFP vs $Pgk^{M.x.}$-sfGFP	0.33
$AcnA^{E.c.}$-sfGFP vs $AcnA^{Y.e.}$-sfGFP	0.093
$AcnA^{E.c.}$-sfGFP vs $AcnA^{V.c.}$-sfGFP	0.084
$AcnA^{E.c.}$-sfGFP vs $AcnA^{M.x.}$-sfGFP	0.0000000023
$AcnA^{E.c.}$-sfGFP vs $AcnA^{B.s.}$-sfGFP	0.069

129 **Figure 1 – figure supplement 7B**

Testing pair	*P-value*
$Adk^{E.c.}$-sfGFP vs $Adk^{Y.e.}$-sfGFP	0.000060
$Adk^{E.c.}$-sfGFP vs $Adk^{V.c.}$ -sfGFP	0.18
$Adk^{E.c.}$-sfGFP vs $Adk^{C.c.}$-sfGFP	0.042
$Adk^{E.c.}$-sfGFP vs $Adk^{M.x.}$-sfGFP	0.070
$Adk^{E.c.}$-sfGFP vs $Adk^{B.s.}$-sfGFP	0.0029
$Pgk^{E.c.}$-sfGFP vs $Pgk^{V.c.}$-sfGFP	0.11
$Pgk^{E.c.}$-sfGFP vs $Pgk^{C.c.}$-sfGFP	0.0082
$Pgk^{E.c.}$-sfGFP vs $Pgk^{M.x.}$-sfGFP	0.0087
$AcnA^{E.c.}$-sfGFP vs $AcnA^{Y.e.}$-sfGFP	0.035
$AcnA^{E.c.}$-sfGFP vs $AcnA^{V.c.}$-sfGFP	0.16
$AcnA^{E.c.}$-sfGFP vs $AcnA^{M.x.}$-sfGFP	0.083
$AcnA^{E.c.}$-sfGFP vs $AcnA^{B.s.}$-sfGFP	0.00024

130

131 **Figure 2C**

Testing pair	*P-value*
Untreated vs A22 treatment	0.00000000000032

132

133 **Figure 2D**

Testing pair	*P-value*
Untreated vs A22 treatment	0.0022

134

135 **Figure 4A**

Testing pair	*P-value*
sfGFP 25°C vs 35°C	0.000040
Adk-sfGFP 25°C vs 35°C	0.0000025
AcnA-sfGFP 25°C vs 35°C	0.00077

136

137 **Figure 4B**

Testing pair	*P-value*
sfGFP Untreated vs Chloramphenicol	0.61
sfGFP DMSO vs Rifampicin	0.012
Adk-sfGFP Untreated vs Chloramphenicol	0.12
Adk-sfGFP DMSO vs Rifampicin	0.00048
Pgk-sfGFP Untreated vs Chloramphenicol	0.17
Pgk-sfGFP DMSO vs Rifampicin	0.0000012
AcnA-sfGFP Untreated vs Chloramphenicol	0.000011
AcnA-sfGFP DMSO vs Rifampicin	0.0085

138

139

140

141 **Figure 4 – figure supplement 1**

Testing pair	*P-value*
sfGFP ionic strength 105 mM vs 305 mM	0.000027

142

143 **Figure 4 – figure supplement 2**

Testing pair	*P-value*
sfGFP Grown 25°C, measured 25°C vs 35°C	0.0020
sfGFP Measured 25°C, grown 25°C vs 37°C	0.060
sfGFP Measured 35°C, grown 25°C vs 37°C	0.98
sfGFP Grown 37°C, measured 25°C vs 35°C	0.000040

144

145 **Figure 5**

Testing pair	*P-value*
sfGFP M9 salts vs M9 salts, Cam	0.82
sfGFP M9 salts vs M9 salts, Glu+CA	0.000023
sfGFP M9 salts, Cam vs M9 salts, Cam, Glu+CA	0.019
sfGFP M9 salts, Glu+CA vs M9 salts, Cam, Glu+CA	0.019
AcnA-sfGFP M9 salts vs M9 salts, Cam	0.37
AcnA-sfGFP M9 salts vs M9 salts, Glu+CA	0.0073
AcnA-sfGFP M9 salts, Cam vs M9 salts, Cam, Glu+CA	0.0035
AcnA-sfGFP M9 salts, Glu+CA vs M9 salts, Cam, Glu+CA	0.014

146

147

148

149

150

151

152

153

Appendix 5

Numerosity of the constructs and conditions for each experiment

Table 1. Figure 1 and Figure 1 – figure supplement 4 and 6

Construct	*Numerosity (n)*	*Construct*	*Numerosity (n)*
sfGFP	42	Pgk-sfGFP	16
YggX-sfGFP	8	EntC-sfGFP	15
ClpS^{WT}-sfGFP	11	AroA-sfGFP	9
ClpS^{D35A_D36A_H66A}-sfGFP	10	ThrC-sfGFP	14
FolK-sfGFP	8	MurF-sfGFP	7
Crr-sfGFP	14	DsdA-sfGFP	14
UbiC-sfGFP	14	HemN-sfGFP	13
CoaE-sfGFP	11	PrpD-sfGFP	12
Adk-sfGFP	23	DnaK^{WT}-sfGFP	10
Cmk-sfGFP	16	DnaK^{V436F}-sfGFP	10
KdsB-sfGFP	22	MalZ-sfGFP	9
Map^{WT}-sfGFP	20	GlcB-sfGFP	16
Map$^{Lys\rightarrow Glu}$-sfGFP	10	MetE-sfGFP	8
Map$^{Lys\rightarrow Ala}$-sfGFP	12	LeuS-sfGFP	14
MmuM-sfGFP	14	AcnA-sfGFP	19
PanE-sfGFP	18	MetH-sfGFP	9
SolA-sfGFP	7		

Table 2. Figure 1 – figure supplement 7

Construct	*Numerosity (n)*	*Construct*	*Numerosity (n)*
Adk$^{E.c.}$-sfGFP	Same as table 1	Pgk$^{C.c.}$-sfGFP	5
Adk$^{Y.e.}$-sfGFP	5	Pgk$^{M.x.}$-sfGFP	11
Adk$^{V.c.}$-sfGFP	10	AcnA$^{E.c.}$-sfGFP	Same as table 1
Adk$^{C.c.}$-sfGFP	5	AcnA$^{Y.e.}$-sfGFP	5
Adk$^{M.x.}$-sfGFP	11	AcnA$^{V.c.}$-sfGFP	10
Adk$^{B.s.}$-sfGFP	10	AcnA$^{M.x.}$-sfGFP	10
Pgk$^{E.c.}$-sfGFP	Same as table 1	AcnA$^{B.s.}$-sfGFP	10
Pgk$^{V.c.}$-sfGFP	10		

Table 3. Figure 2C and 2D

Condition	*Numerosity (n)*
Untreated	10
A22-treated	12

165 **Table 4. Figure 3**

Construct	*Numerosity (n)*	*Construct*	*Numerosity (n)*
sfGFP	11	DsdA-sfGFP	10
YggX-sfGFP	10	GlcB-sfGFP	10
Adk-sfGFP	16	AcnA-sfGFP	10
PanE-sfGFP	11	MetH-sfGFP	15

166

167 **Table 5. Figure 4A**

Construct and condition	*Numerosity (n)*	*Construct and condition*	*Numerosity (n)*
sfGFP, 25°C	See table 1	AcnA-sfGFP, 25°C	See table 1
sfGFP, 35°C	14	AcnA-sfGFP, 35°C	18
Adk-sfGFP, 25°C	See table 1		
Adk-sfGFP, 35°C	21		

168

169 **Table 5. Figure 4B**

Construct and condition	*Numerosity (n)*	*Construct and condition*	*Numerosity (n)*
sfGFP, untreated	See table 1	Pgk-sfGFP, untreated	See table 1
sfGFP, chloramphenicol	10	Pgk-sfGFP, chloramphenicol	10
sfGFP, DMSO	15	Pgk-sfGFP, DMSO	10
sfGFP, rifampicin	15	Pgk-sfGFP, rifampicin	10
Adk-sfGFP, untreated	See table 1	AcnA-sfGFP, untreated	See table 1
Adk-sfGFP, chloramphenicol	10	AcnA-sfGFP, chloramphenicol	10
Adk-sfGFP, DMSO	10	AcnA-sfGFP, DMSO	10
Adk-sfGFP, rifampicin	10	AcnA-sfGFP, rifampicin	10

170

171 **Table 6. Figure 4 – figure supplement 1**

Construct and condition	*Numerosity (n)*
sfGFP, 105 mM ionic strength	See table 1
sfGFP, 305 mM ionic strength	11

172

173 **Table 6. Figure 4 – figure supplement 2**

Construct and condition	*Numerosity (n)*
sfGFP, grown 25°C, measured 25°C	10
sfGFP, grown 25°C, measured 35°C	10
sfGFP, grown 37°C, measured 25°C	See table 1
sfGFP, grown 37°C, measured 35°C	See table 5

174

175

176

177

178

179 **Table 7. Figure 5**

Construct and condition	*Numerosity (n)*	*Construct and condition*	*Numerosity (n)*
sfGFP, M9 salts	10	AcnA-sfGFP, M9 salts	5
sfGFP, M9 salts, Cam	13	AcnA-sfGFP, M9 salts, Cam	8
sfGFP, M9 salts, Glu+CA	15	AcnA-sfGFP, M9 salts, Glu+CA	10
sfGFP, M9 salts, Cam, Glu+CA	13	AcnA-sfGFP, M9 salts, Cam, Glu+CA	10

180

181